Available online at www.sciencedirect.com
ScienceDirect
International Journal of Mass Spectrometry 261 (2007) 115–133
International Journal of Mass Spectrometry
www.elsevier.com/locate/ijms

Investigation of the accuracy of ion optics simulations using Kepler orbits in a spherical capacitor

T.J.M. Zouros [a,b,*], Omer Sise [c], F.M. Spiegelhalder [a,1], David J. Manura [d]

[a] *Department of Physics, University of Crete, P.O. Box 2208, 71003 Heraklion, Crete, Greece*
[b] *Institute of Electronic Structure and Laser, P.O. Box 1527, 71110 Heraklion, Crete, Greece*
[c] *Department of Physics, Science and Arts Faculty, Afyon Kocatepe University, Afyonkarahisar 03200, Turkey*
[d] *Scientific Instrument Services, Inc., Ringoes, NJ, USA*

Received 10 July 2006; received in revised form 12 August 2006; accepted 12 August 2006
Available online 4 October 2006

Abstract

Benchmark evaluations of the accuracy of SIMION 3D, a finite difference ion optics package, are presented for electron motion in a spherical capacitor (SC) or ideal hemispherical deflector analyzer (HDA). The fractional errors (FE) [FE ≡ (simulation-exact)/exact] for potential, electric field, trajectory radius and time-of-flight (TOF) are characterized in detail over a wide range of systems and include comparisons of Monte Carlo generated line shapes at the first-order focusing plane. Simple theoretical models based on a first-order perturbation treatment are provided to explain, predict, and even correct the trajectory radius and TOF errors over the central region of any HDA. Our results are summarized in tables, scaling formulas, and practical guidelines.

PACS: 07.81.+a, 41.20Cv, 41.85, 29.30.Dn

Keywords: Electron-optics simulations; Hemispherical analyzers; Ray tracing; Finite differences; SIMION; Electron spectroscopy

1. Introduction

Simulating the trajectories of charged particles, such as electrons and ions, is an indispensable aid in the design and testing of experimental devices such as energy analyzers and time-of-flight (TOF) spectrometers. However, for the results to be trustworthy, the limitations and accuracy of such simulations must be well understood and tested. A simple way to evaluate this accuracy is to simulate a trajectory that can be independently calculated to high accuracy, such as one that can be solved analytically. Kepler orbits of charged particles in a spherical capacitor (SC) is one such example [1]. The SC (see Fig. 1) has the advantage that it is a closed system with well-defined electrode boundaries, it does not suffer from fringing fields, and non-relativistic trajectories are analytically described. More practically, the electrostatic field in an SC is identical to that of an *ideal* hemispherical deflector analyzer (HDA), thereby making the SC ideally suited for benchmark evaluations of the accuracy of ion optics simulations [1–4] of an HDA.

HDAs are often simulated by various ion optics packages such as SIMION 3D [5], CPO-3D [6] and OPERA [7], to name a few. In our laboratories, we have used SIMION 3D extensively to simulate lenses [8] and HDAs [9] for electron spectroscopy because of its relatively low cost and ease of use. However, no detailed information on the accuracy and limitation of simulations pertaining specifically to HDAs is available. Cubric et al. [1] have used an SC, as well as other electrode configurations, to report general benchmark intercomparisons of computational accuracy versus computational speed for various ion-optics simulation approaches. Dahl [3] also gave some rather general limits on the accuracy of SIMION 3D kinematics and reported on trajectory evaluations for motion in an ideal cylindrical mirror analyzer. The inherent geometric limitation in the modeling of curved electrode surfaces by fixed-size square (2-D) or cubic (3-D) unit constructs, as used in finite difference packages such as SIMION, can be a limiting factor on the accuracy of the particle trajectories. While the effects of mechanical imperfections in electrode geometry construction on the electron-optical proper-

* Corresponding author. Tel.: +30 2810 394117; fax: +30 2810 394101.
E-mail address: tzouros@physics.uoc.gr (T.J.M. Zouros).
[1] Present address: IQOQI, Austrian Academy of Sciences, Innsbruck, Austria.

1387-3806/$ – see front matter © 2006 Elsevier B.V. All rights reserved.
doi:10.1016/j.ijms.2006.08.005

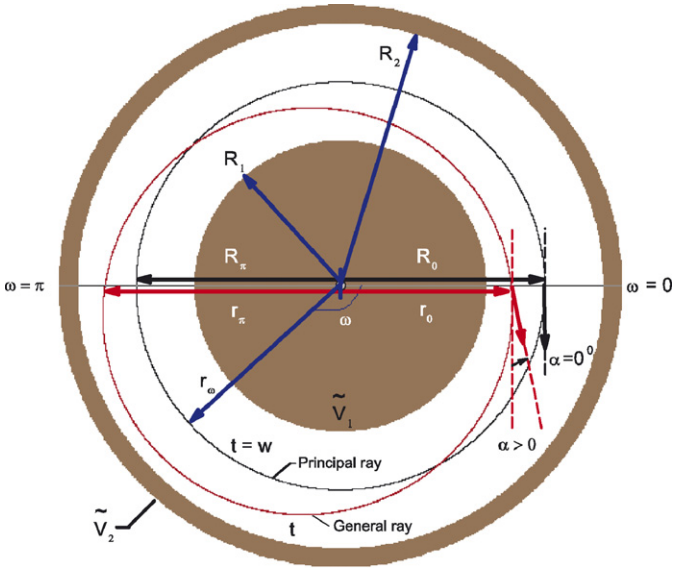

Fig. 1. (Color on line) Cross sectional view of the spherical capacitor. The principal ray launched at radius R_0, with kinetic energy $K_0(= \mathrm{w})$ and angle $\alpha = 0^\circ$ goes through R_π at the first-order focusing plane ($\omega = 180^\circ$). The values of the radii R_0, R_π, the potential $\tilde{V}_0 = \tilde{V}(R_0)$ and pass energy w determine the SC voltages $\tilde{V}_1$, $\tilde{V}_2$. A general ray launched at $r_0 < R_0$ with pass energy $t > \mathrm{w}$ and $\alpha > 0^\circ$ is also shown.

ties of an HDA have been investigated [10,11], no such analysis has been attempted to our knowledge for simulated electrode geometries.

Here, we investigate the accuracy of simulated SC trajectories and its dependence on the electrode modeling error. Specifically, we report on detailed benchmark evaluations of the accuracy of SIMION 3D v.7 [5] using an SC with a mean radius $\bar{R} = 101.6\,\mathrm{mm}$, typical of fairly large HDAs [12] and used in our laboratory for Auger spectroscopy of ion–atom collisions [13–15]. Characteristic SC parameter values used are given in Table 1. We first determine the accuracy of the simulated potential, electric field, electron trajectory radius and TOF for various well specified trajectories, presenting these in the form of fractional errors (FE) as a function of the orbit angle ω. For $\omega = \pi$, the HDA first-order focus plane of particular importance to electron spectroscopy, point source line shapes are also generated using Monte-Carlo techniques and compared. We then examine how the trajectory radius and TOF FEs depend in a predictable way on the interradial electrode spacing $\rho \equiv (R_2 - R_1)/\bar{R}$ for $\rho = 0.18 - 0.97$ and simulation grid densities $\lambda = 1 - 10\,\mathrm{gu/mm}$. Finally, using the generated FE data we present and test simple theoretical models within the context of a first-order perturbational approach to relate the electrode modeling errors to the SIMION trajectory FEs for the central trajectories, predicting their values to within about ±5%. A brief, but complete, introduction of Kepler orbits in an ideal SC is included together with a short description of SIMION. Further details are delegated to the two appendices.

These results should be of direct practical use primarily to investigators trying to model the electron-optical properties of HDAs using SIMION 3D generated trajectories. However, our methodology, benchmark evaluations, analysis and theoretical modeling should also be of more general interest to the extended charged particle optics community.

Table 1
SC dimensions and associated parameters of the principal ray describing a circle of radius $R_0 = \bar{R} = 101.6\,\mathrm{mm}$, pass energy $\mathrm{w} = 1000\,\mathrm{eV}$ and unbiased entry potential $\tilde{V}_0 \equiv \tilde{V}(R_0) = 0$

Mean radius (mm)	$\bar{R}$	101.6
Radius inner sphere (mm)	R_1	72.4
Radius outer sphere (mm)	R_2	130.8
ΔR (mm)	$R_2 - R_1$	58.4
Interradial electrode spacing ρ	$\Delta R/\bar{R}$	0.5748
Voltage inner sphere (V)	$\tilde{V}_1$	806.6298
Voltage outer sphere (V)	$\tilde{V}_2$	−446.4832
$\Delta\tilde{V}$ (V)	$\tilde{V}_2 - \tilde{V}_1$	−1253.113
Potential constant (V-mm)	k	−203200
Potential constant (V)	c	−2000
$\tilde{\mathcal{E}}_\mathrm{r}$ (V/mm)	$-\frac{\Delta\tilde{V}}{\Delta\bar{R}}$	21.4574
Principal ray:		
Total energy (eV)	E_0	−1000
Kinetic energy at R_0 (eV)	K_0	1000
Semi-major axis length (mm)	a_0	101.6

2. Theory

We begin with a very brief introduction to the theoretical treatment of trajectories within the $1/r$ potential (Kepler orbits) of an SC or ideal HDA [16]. The equations presented here for the potential, electric field, trajectory radius, and TOF are then used throughout the paper without further explanation. More detailed and specialized results needed in our investigation are presented in Appendix A.

2.1. Trajectory equations in the ideal $1/r$ potential

The potential $\tilde{V}(r)$ and radial electric field $\mathcal{E}_\mathrm{r}$ of an SC (see Fig. 1) are given by

$$\tilde{V}(r) = \tilde{V}(k, c, r) = -k/r + c \tag{1}$$

$$\mathcal{E}_\mathrm{r}(r) = \mathcal{E}_\mathrm{r}(k, r) = -k/r^2 \tag{2}$$

with

$$\vec{\mathcal{E}} = -\vec{\nabla}\tilde{V} = \mathcal{E}_\mathrm{r}\hat{r} \tag{3}$$

For voltages $\tilde{V}_i \equiv \tilde{V}(R_i)$ $(i = 1, 2)$ used on the SC electrodes, the constants k and c can be directly evaluated from Eq. (1):

$$c \equiv c(R_1, R_2) = \frac{R_2\tilde{V}_2 - R_1\tilde{V}_1}{\Delta R} \tag{4}$$

$$k \equiv k(R_1, R_2) = \frac{\Delta\tilde{V}}{\Delta R} R_1 R_2 \tag{5}$$

with $\Delta R \equiv R_2 - R_1$, $\Delta\tilde{V} \equiv \tilde{V}_2 - \tilde{V}_1$.

The orbit of a particle with charge q inside the SC is in general an ellipse (Kepler orbit) and can be parameterized by the angle ω over a complete orbit. For a particle launched at $\omega = 0^\circ$ with radius r_0, kinetic energy $K(r_0) = (1/2)\,m\,v_0^2$ and launching velocity angle α, the elliptical orbit will be characterized by its semi-major axis a, its eccentricity ϵ and the conserved *total* particle energy $E < 0$. The *non-relativistic* trajectory, radius r_ω

and TOF T_ω, have been derived in detail in ref. [16] and have the simple functional form:

$$r_\omega = r_\omega(k) \equiv r(r_0, \eta_k, \alpha; \omega) = \frac{r_0}{[(1-\cos\omega)/((1+\eta)\cos^2\alpha)] + \cos\omega - \tan\alpha\sin\omega} \tag{6}$$

$$T_\omega = T_\omega(k) \equiv T(r_0, \eta_k, \alpha; \omega) = r_0\sqrt{\frac{m\,r_0}{q\,k}}\,(1+\eta)^{3/2}\,\cos^3\alpha\,I(\eta,\alpha,\omega) \tag{7}$$

where the parameter $\eta \equiv \eta_k = \eta(r_0, q\,k, K)$ and the integral $I(\eta, \alpha, \omega)$ are given by:

$$\eta(r_0, q\,k, K) \equiv 1 - \frac{r_0}{a} = \frac{2\,r_0\,K(r_0)}{q\,k} - 1 \tag{8}$$

$$I(\eta,\alpha;\omega) \equiv \int_0^\omega \frac{\mathrm{d}\omega'}{[1-(1-\eta)\cos\alpha\cos(\alpha+\omega') + \cos(2\alpha+\omega')]^2} \tag{9}$$

and the elliptical orbit parameters by [16]:

$$a = -\frac{q\,k}{2\,E} \qquad \text{(semi-major axis)} \tag{10}$$

$$E = K(r_0) - \frac{q\,k}{r_0} \qquad \text{(conserved total energy)} \tag{11}$$

$$\epsilon = \sqrt{\sin^2\alpha + \eta^2\cos^2\alpha} \qquad \text{(eccentricity)} \tag{12}$$

The angle α determines the direction of the velocity vector $\vec{v}_0$ relative to the orbit radius $\vec{r}_0$ at the launching point with $\omega = 0^\circ$ [16]:

$$\sin\alpha \equiv \frac{\vec{v}_0 \cdot \vec{r}_0}{v_0\,r_0} \tag{13}$$

For $\alpha = 0^\circ$, the two vectors are perpendicular to one another and the particle is at its smallest orbit radius or periapse [16]. We note that the conserved total energy E is always negative for bound motion and depends only on k. Thus, particle motion inside the SC is independent of the potential constant c. Adding a constant voltage V to both $\tilde{V}_1$ and $\tilde{V}_2$, increases c by V (see Eq. (4)) but does not affect the value of k (see Eq. (5)), and therefore the trajectories remain unchanged.

When the eccentricity is zero, i.e. $\epsilon = 0$, much simpler *circular* orbits result. Directly from Eq. (12), both conditions $a = r_0$ ($\eta = 0$) and $\alpha = 0^\circ$ must apply simultaneously and therefore:

$$\textit{Circular orbits}: \quad \epsilon = 0, \qquad a = r_0, \quad \alpha = 0, \tag{14}$$

$$E = -K(r_0), \qquad K(r_0) = \frac{q\,k}{2\,r_0}, \qquad \eta = 0 \tag{15}$$

$$r_\omega = r_0 \tag{16}$$

$$T_\omega = r_0\,\omega\sqrt{\frac{m}{2\,K(r_0)}} \tag{17}$$

For electrons ($q = -e$), with the $m = m_e = 5.485799030 \times 10^{-4}$ amu, we then have for circular orbits the practical formula:

$$T_\omega = 2.942738 \times 10^{-2}\ \text{ns}\ \left[\frac{r_0(\text{mm})\,\omega(\text{dgrs})}{\sqrt{K(r_0)(\text{eV})}}\right] \tag{18}$$

The voltages $\tilde{V}_1$ and $\tilde{V}_2$ are determined by "tuning" the SC to a particular reference trajectory known as the *principal* ray [16] (see Fig. 1). Here, we shall limit our investigation to conventional HDA usage, always taking the principal ray to be a *circle* of radius $R_0 = \bar{R}$ with entry potential $\tilde{V}(R_0) = 0$. Then, according to Eq. (A.17) of Appendix A the SC voltages for electrons are given by:

$$\tilde{V}_i = 2\,\text{w}\left(\frac{\bar{R}}{R_i} - 1\right) \qquad (i = 1, 2) \tag{19}$$

In this paper we shall always use a pass energy w = 1000 eV and $\bar{R} = 101.6$ mm for which potential constants k and c (Eqs. (4) and (5)) are always fixed to the same values, i.e. $k = -203200$ and $c = -2000$, even when varying the SC interradial electrode spacing ρ (see Section 5.3). Orbits with three different entry radii r_0 are investigated. The values of the SC parameters and trajectory variables for circular orbits (I, II and III) used in our evaluation of SIMION accuracy are listed in Tables 1 and 2.

3. Experimental method—SIMION

SIMION is a powerful, user-friendly ion-optics PC software used to calculate electric and/or magnetic fields (quasi-static) from user-supplied geometries and to simulate the trajectories of charged particles flying through those fields. SIMION has become very popular and is widely used as an aid in the design of spectrometer components and lens systems (for some recent examples see [8,17–29]). For more details, the interested reader is referred to the SIMION manual [5,30] and associated literature [3].

SIMION makes use of potential arrays (PA), which define fixed-sized square (2-D geometry) or cubic (3-D geometry) grids of elements on which electrodes are represented (see Fig. 2 top). The potential on each electrode point must be defined by the user, while the resulting potentials of the grid points between the electrodes are calculated by SIMION which solves the Laplace equation using an optimized over-relaxation finite difference approach (refining process). The electric field vector is then computed by taking the gradient of the calculated potential. SIMION's finite difference techniques use the average potential of the nearest four (2-D geometry) or six (3-D geometry) neighboring grid units as the basis for estimating the potential of each non-electrode point, so numerical results could differ slightly depending on the 2-D, 3-D, or symmetry representation used. A workbench strategy allows different PA sizes, symmetries, and grid densities to be used in the same simulation. After the fields are solved, charged particles – given launching position, kinetic energy and direction – can be readily flown through space with their trajectories computed *relativistically* using accurate fourth-order Runge-Kutta techniques.

In the first part of this investigation, we examine the SC system described in Table 1 when modeled in three distinct ways

Table 2
Theoretical electron trajectory parameters for circular orbits I, II and III having $\alpha = 0^\circ$ and $a = r_0$ in the field of the spherical capacitor specified in Table 1

		Circular orbit		
		I	II	III
Radius (mm, Eq. (6))	r_0	81.6	101.6	121.6
Kinetic energy (eV, Eq. (15))	$K(r_0)$	1245.098	1000	835.5263
Potential (V, Eq. (1))	$\tilde{V}(r_0)$	490.1961	0	−328.9474
$\mathcal{E}_r$-field (V/mm, Eq. (2))	$\mathcal{E}_r(r_0)$	30.5171	19.6850	13.7422
Total energy (eV, Eq. (15))	E	−1245.098	−1000	−835.5263
TOF ($\omega = 180^\circ$) (ns, Eq. (17))	T_π	12.2493	17.0183	22.2831
TOF ($\omega = 360^\circ$) (ns, Eq. (17))	$T_{2\pi}$	24.4985	34.0366	44.5662

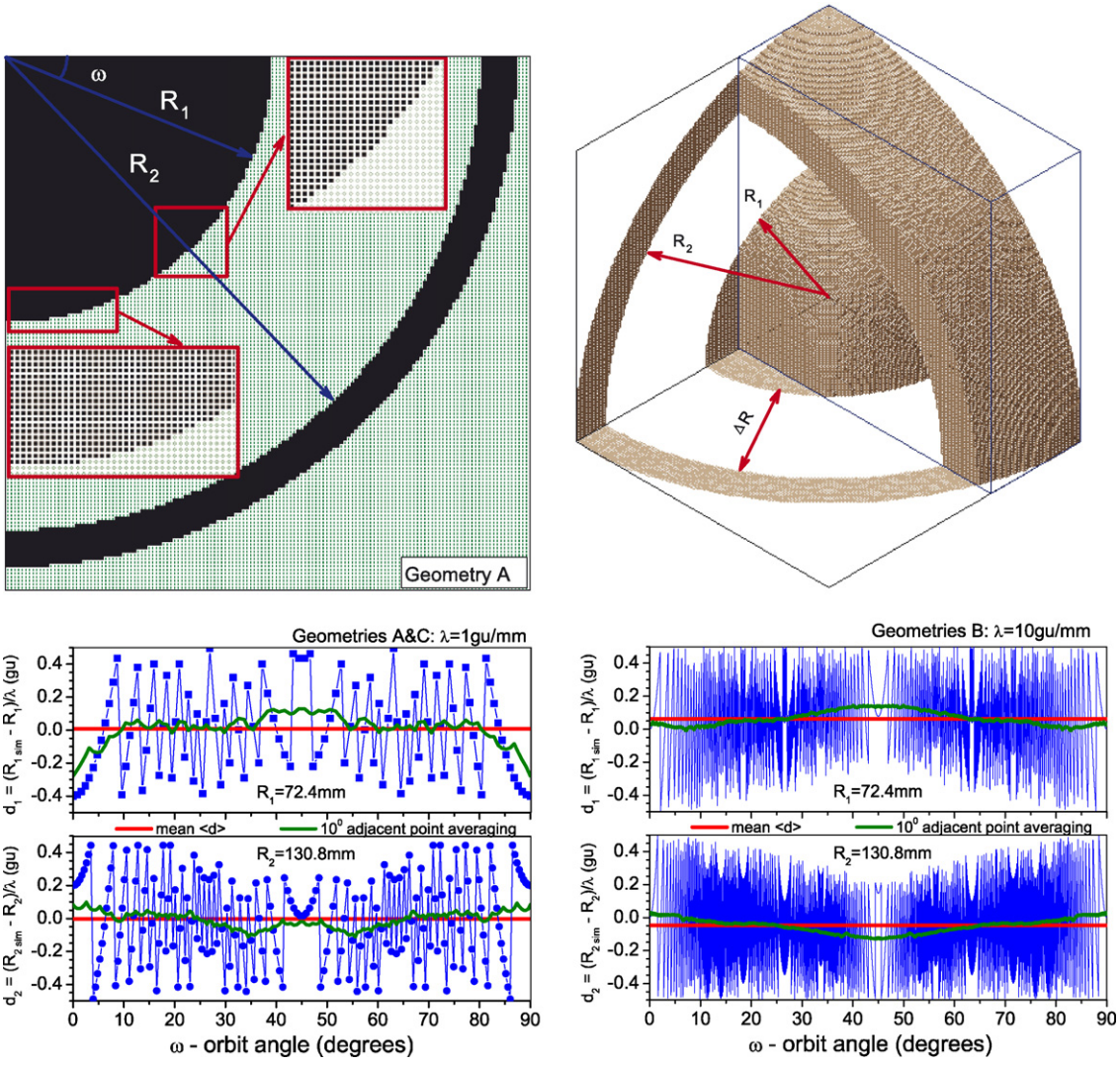

Fig. 2. (Color on line) SIMION electrode geometries. (Top) Left: geometries A and B—SC modeled with 2-D quarter circle in XY plane. (Top) Right: geometry C—SC modeled with 3-D eighth of sphere in positive octant. The cross-section of the 3-D figure in the XY ($Z = 0$) plane is identical to the 2-D figure. Of special concern in this investigation is the inherent error introduced by the modeling of curved electrodes by squares (2-D geometry) or cubes (3-D geometry) and its effect on the particle trajectories. In the inserts (top left), a more detailed look of two parts of the inner electrode surface construction of geometry A is shown. (Bottom) Left: variation of surface radii errors $d_{1,j}$, $d_{2,j}$ with ω for geometry A. Geometry C results, not shown, are similar. The mean values are $\langle d_1 \rangle = 0.0017$ gu and $\langle d_2 \rangle = 0.0018$ gu, shown as the red straight lines in the plot and listed in Table 5 (nw). The green wavy lines are smoothed $\pm 5^\circ$ adjacent point averages. Due to the symmetric way the electrodes are generated the observed structure is exactly repeated every 90°. (Bottom) Right: same as left but for geometry B with $\langle d_1 \rangle = 0.0619$ gu and $\langle d_2 \rangle = -0.0459$ gu. The standard deviations in $d_{i,j}$ used in the quadrature error propagation model are very close to 0.26 ± 0.1 gu and are also listed in Table 5 (quad).

Table 3
Specifications of the SIMION electrode design geometries A, B and C

	Geometry		
	A	B	C
Dimensionality	2-D	2-D	3-D
PA symmetry/mirroring[a],[b]	c/*xy*	c/*xy*	p/*xzy*
Grid density λ (gu/mm)	1	10	1
Grid dimensions (gu)	150	1500	150
PA size (kB)	176	17579	26368

The corresponding SIMION geometry files are listed in Appendix B.1.

[a] Symmetries: c, cylindrical around *x*-axis; p, planar.
[b] Mirroring: enabled in *x*, *y*, *z* directions.

– referred to as geometries A, B and C – shown in Table 3 and the SIMION geometry files in Appendix B.1. Geometries A and B are 2-D representations, B using ten times higher grid density (grid units (gu) per mm) than A, whereas geometry C is a 3-D representation. The 2-D models contain two concentric quarter-circles lying in the positive quadrant of the XY ($Z = 0$) plane (see Fig. 2 top), which when mirrored in the negative x direction and subsequently rotated through 360° around the x-axis (cylindrical symmetry) represent the two full spheres. The 3-D models utilize two concentric one-eighth spheres (positive octant), which when mirrored in all three negative x, z and y directions represent the two full spheres as well.

With these settings, electrons were "flown" in the equatorial ($Z = 0$) XY plane in all three geometries A, B and C and launched at $\omega = 0°$, with $x_{\rm sim} = x = r_0$, $y_{\rm sim} = y = 0$, kinetic energy $K_{\rm sim}(r_0) = K(r_0)$ and injection angle α set through SIMION velocity elevation angle Elv $= -90° \pm \alpha$ and azimuth angle Azm $= 0°$ (see Fig. 1). While flying the electrons, SIMION recorded all required data at each time-step $T_{\rm sim}$ into a file for evaluation. The values recorded were the position coordinates $x_{\rm sim}$ and $y_{\rm sim}$, from which the radius $r_{\rm sim}$ and the orbit angle ω were calculated according to Eqs. (25) and (26), the time-of-flight $\mathrm{TOF}_{\rm sim}(\omega)$ and the kinetic energy error $\Delta K_{\rm sim}(\omega)$. ΔK measures change in total energy, ideally zero under conservation of energy, so a non-zero value indicates simulation error. All theoretical parameters were calculated according to the equations presented in Section 2 and Appendix A using the official 2002 CODATA recommended values [31] for 1 amu = 931,494,043 eV and the speed of light = 299.7924580 mm/ns, also used by SIMION.

One of the main goals of this paper is to quantify the electrode surface modeling errors and use them to predict the errors seen in the trajectories. We note that the particular geometries A, B and C chosen for this study are representative of typical SIMION usage and, in particular, demonstrate clearly the effect of the curved electrode inaccuracies on the trajectories. However, as noted by Dahl [3] in his investigation of the cylindrical mirror analyzer, improved accuracy can be attained by judicious choice of symmetry and integrally aligned electrode boundaries to minimize or eliminate the modeling error in the electrodes. As investigated in Appendix B.5, such an approach is only partly possible with the SC, and gives limited improvement, by using cylindrical symmetry with integrally aligned electrodes in the $X = 0$ plane (geometry B) and flying electrons in the $X = 0$ plane. We instead concentrate the main part of this study on the more general case of flying electrons in the $Z = 0$ plane where no such alignment is possible, even with cylindrical symmetry.

The modeling error can be computed at each point j on the electrode surface and is defined by $\Delta R_{i,j} \equiv R_{i\,{\rm sim}_j} - R_i$ (for surface $i = 1, 2$), or in grid units by $d_{i,j} \equiv \Delta R_{i,j}\lambda$. Here, $R_{i\,{\rm sim}_j}$ is the radial distance from the origin to point j in the simulated model, and R_i are the nominal (theoretical) values of the SC radii given in Table 1. The values of $R_{i\,{\rm sim}_j}$ (Fig. 2 top) can be readily extracted from the SIMION potential array by measuring the radial distance to each surface electrode point. We have taken a more convenient approach of computing these values theoretically from the same discretized equation of the sphere that SIMION uses to generate the potential array in the first place (*circle* or *sphere* commands in the .gem files in Appendix B.1). This is automated using PERL script `sc_list_surface_points.pl`. Our script first defines the "surface count" of a given electrode grid point as the number of non-electrode grid points that are orthogonally adjacent to it. Thus, a surface count of 0–4 (for 2-D geometries) or 0–6 (for 3-D geometries) can be assigned to any grid point. A grid point with a surface count of zero is ignored because it lies just away from the surface and is invisible to the four-point (2-D geometries) or six-point (3-D geometries) finite difference methods, which look only at the orthogonally adjacent points. The code compiles a list of all grid points (x_j, y_j, z_j) with non-zero surface count, thereby constituting the set of all "surface points" S. For each such point $j \in S$ the surface radius, $R_{i\,{\rm sim}_j}$ ($i = 1$ or 2), is computed as $R_{i\,{\rm sim}_j} = \sqrt{x_j^2 + y_j^2 + z_j^2}$ and the angle ω_j in the $Z = 0$ plane can also be assigned using $\omega_j = \arctan(y_j/x_j)$ as shown in Fig. 2 (top).

As an illustration of the above procedure we show in Fig. 2 (bottom) examples of the variation in the modeling errors $d_{i,j}$ as a function of ω together with their means $\langle d_i \rangle$ in the $Z = 0$ plane. A ±5° running average (green line) is included to make the general trends more clear. The same variation pattern is repeated every 90° as expected from the symmetry in the models already shown in Fig. 2 (top). The modeling errors are seen to be small with their mean very near zero (thick red line) and their variations bounded within ±0.5 gu, indicating that the SIMION geometry file parameters in Appendix B.1 are indeed well chosen. The most significant sustained departures from zero are seen to occur at $\omega = 0°$, 45° and 90°. At these angles the simulated potential and electric field (given later in Section 5.1.1) show their largest departures from theory and constitute one of the chief causes of error accumulation in the trajectory.

4. Computed fractional errors

SIMION's results (identified by the subscript 'sim') are recorded and compared to theory by presenting them in the form of "normalized" fractional errors [1,3]. FE definitions for the potential V, radial electric field $\mathcal{E}_{\rm r}$, trajectory radius r_ω, TOF T_ω and kinetic energy error ΔK are given below:

$$\mathrm{FE}_V(\omega) \equiv \frac{\tilde{V}_{\rm sim}(r_{\rm sim}(\omega)) - \tilde{V}(r_{\rm sim}(\omega))}{\Delta\tilde{V}} \tag{20}$$

$$\mathrm{FE}_{\mathcal{E}_r}(\omega) \equiv \frac{\mathcal{E}_{r_{sim}}(r_{sim}(\omega)) - \mathcal{E}_r(r_{sim}(\omega))}{\mathcal{E}_r(r_{sim}(\omega))} \quad (21)$$

$$\mathrm{FE}_r(\omega) \equiv \frac{r_{sim}(\omega) - r_\omega}{r_\omega} \quad (22)$$

$$\mathrm{FE}_{TOF}(\omega) \equiv \frac{10^{-6}T_{sim}(\omega) - T_\omega}{T_\pi} \quad (23)$$

$$\mathrm{FE}_{\Delta K}(\omega) \equiv \frac{\Delta K_{sim}(\omega)}{K_{sim}(r_{sim}(\omega))} \quad (24)$$

$$r_{sim}(\omega) = \sqrt{x_{sim}^2 + y_{sim}^2} \quad (25)$$

$$\omega \equiv \tan^{-1}(y_{sim}/x_{sim}) \quad (26)$$

$\tilde{V}(r)$, $\mathcal{E}_r(r)$, r_ω and T_ω are the exact theoretical functions given analytically in Eqs. (1), (2), (6) and (7), respectively. On the other hand, $\tilde{V}_{sim}(r)$, $\mathcal{E}_{r_{sim}}(r)$, r_{sim} and TOF_{sim} are the directly "measurable" SIMION quantities that will be used to test all proposed theoretical models.

All FEs are defined as the difference between the SIMION computed quantity and its exact (theoretical) value divided by a normalization value, often the theoretical value. This normalization value is different in each case. In particular, the potential FE was normalized to the difference $\Delta\tilde{V}$ since $\tilde{V}$ itself can be zero (e.g. $\tilde{V}_0 = 0$ – also note the sign as $\Delta\tilde{V}$ is negative for electrons.) The TOF FE is normalized to the TOF for 180° deflection, T_π. Furthermore, the factor 10^{-6} (see Eq. (23)) corrects the SIMION TOF for the 10^{12} heavier electron mass (and therefore 10^6 times slower) used in the simulation to avoid the relativistic corrections normally applied by SIMION (see Appendix B.2) but not included in the exact theoretical treatment.

5. Results

We now present our data, the computed fractional errors as a function of the angle ω for circular and elliptical trajectories. The data will be compared to the theoretical models developed later on in Section 6.

5.1. Circular orbits with $r_0 = 81.6, 101.6, 121.6$ mm and $\rho = 0.5748$

The computed FEs for SIMION SC geometries A, B and C are presented in Figs. 3 and 4 as functions of ω for the circular orbits I, II and III (Table 2). The same pattern is repeated exactly every 90° (in C) or 180° (in A and B). Errors in the higher grid density geometry B are smaller having smoother electrode surfaces. The observed extrema in FE_V and $\mathrm{FE}_{\mathcal{E}_r}$ can be clearly correlated to one another and to the most significant extrema of the model error $d_{i,j}$ (Fig. 2 bottom), particularly for the lower grid density geometries A and C. The extent to which these extrema affect the trajectory (FE_r and FE_{TOF}) is less obvious. We discuss each FE variation in more detail pointing out the most important features.

5.1.1. Variation of potential and electric field

The potential and radial electric field FEs, FE_V and $\mathrm{FE}_{\mathcal{E}_r}$, show very clear repeated structures every 90° (in C) or 180° (in cylindrical A and B) that are symmetric around the period and half-period marks, as expected from the symmetry used in the SIMION models (see Fig. 2 and Table 3). The sharpest features occur every 90° in the inner-most (near surface, high field) orbit of the low-density geometries A and C. These variations are seen to be clearly correlated to the modeling errors $d_{i,j}$ shown

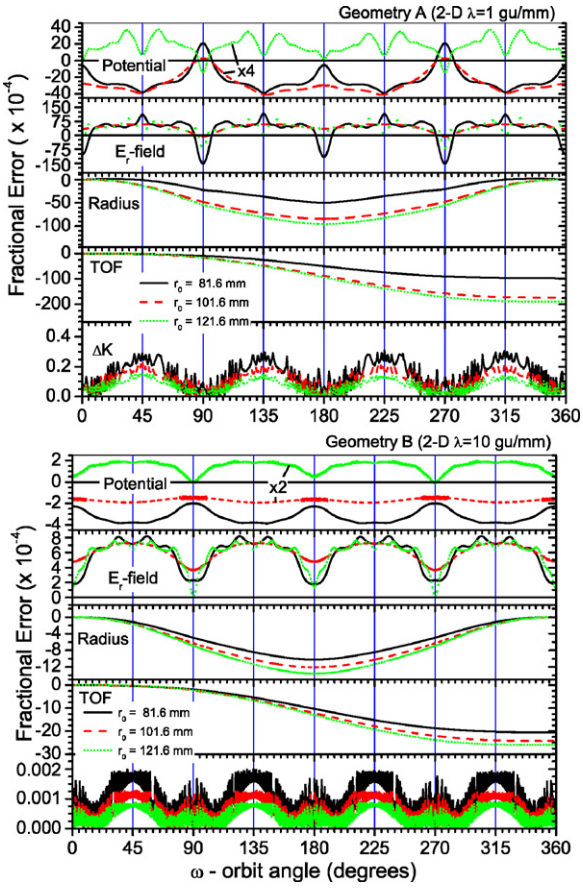

Fig. 3. (Color on line) Fractional errors (FE) in geometry A (top), B (bottom) for the potential, radial electric field, trajectory radius, TOF and kinetic energy error (see Eqs. (20)–(24)) as a function of orbit angle ω. Note the scaling factor used to enlarge various FEs for better viewing. Increasing the grid density λ by a factor of 10 in going from A to B is seen to decrease the fractional variation by roughly the same factor.

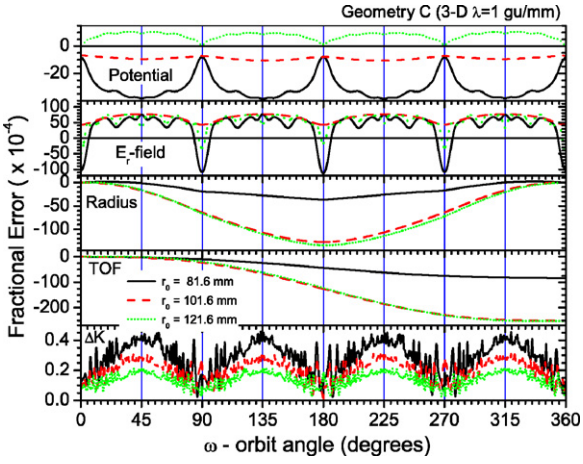

Fig. 4. (Color on line) Same as Fig. 3, but for geometry C.

in Fig. 2 (bottom). In general though, the FE_V values for the two innermost orbits ($r_0 = 81.6$ mm and $r_0 = 101.6$ mm) are negative, while for the outermost orbit ($r_0 = 121.6$ mm) they are positive (note the ×4 and ×2 scaling factors in A and B). Since $\vec{\mathcal{E}} = -\vec{\nabla}V$, this explains the generally positive $FE_{\mathcal{E}_r}$ values. However, particularly for $r_0 = 101.6$ mm, there are also long stretches of constant $FE_{\mathcal{E}_r}$ showing the field to be relatively independent of ω (and also of r as seen later in Fig. 10). This will be an important feature utilized in our theoretical models later on. As we shall see later, the positive value of $FE_{\mathcal{E}_r}$ may be explained by an effective reduction in the fractional interradial electrode spacing ($\rho = \Delta R/\bar{R}$) (see Eqs. (3) and (5)) even though that effect is not easily seen in the direct measurement of modeling errors $d_{i,j}$ in Fig. 2 (bottom).

5.1.2. Variation of trajectory radius

The radial FE, FE_r, is seen to be always negative (orbit radius smaller than theory), as explained by the generally positive $FE_{\mathcal{E}_r}$ values and Eq. (3). $|FE_r|$ increases monotonically from $\omega = 0°$, reaches a maximum near $\omega = 180°$ and then decreases almost, but not exactly, back to zero again at $\omega = 360°$, i.e. it is almost symmetric around $\omega = 180°$. Sharp variations in the electric field along the particle orbit perturb the motion affecting the observed FE_r of the particle, as most strongly seen every 90° in the innermost orbit of A. FE_r is found to be smaller in B than in A and C by factors ranging between ∼ 3 and 15, showing the importance of increasing the grid density λ.

5.1.3. Variation of trajectory TOF

The TOF FE, FE_{TOF}, is also negative in all three geometries, as explained by the negative FE_r and Eq. (17). As in the observation for FE_r, the FE_{TOF} is seen to be smaller in B than in A and C by a factor of ∼ 3–15. Interestingly, at $\omega = 180°$ FE_{TOF} and FE_r appear to be nearly equal, a result we also derive theoretically later on.

5.1.4. Variation of KE

The kinetic energy FE, $FE_{\Delta K}$, is seen to be smaller than all other FEs by at least 3 orders of magnitude, indicating that conservation of energy during trajectory integration is well observed [32,33], in particular for B. Periodic maxima are seen in all three geometries and appear correlated to the minima of FE_V.

5.1.5. Dependence on initial conditions—ω_0 dependence

The variation of the electric field with ω also raises the question of the dependence of the trajectory FEs on the specific starting point ω_0. This dependence can be investigated by evaluating FE_r and FE_{TOF} following a *fixed* length of 180° deflection. Since all orbit calculations are launched at $x = r_0$, $y = 0$ with $\omega = 0°$, in the clockwise direction (see Fig. 1) we have $x(\omega_0) = r_0 \cos\omega_0$, $\quad y(\omega_0) = -r_0 \sin\omega_0$. Our FEs evaluated at $\omega = \omega_0 + \pi$ with ω_0 varying from 0 to 180° are shown in Fig. 5 for motion in the XY ($Z = 0$) plane in the three geometries A, B and C for the principal ray (orbit II $r_0 = 101.6$ mm). At a particular value of ω_0 the radial electric field is given on the left scale, while the values of the radius and TOF FEs after 180° deflection

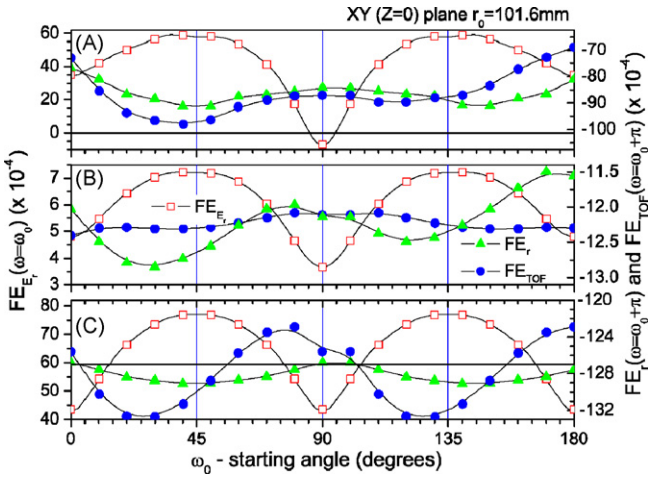

Fig. 5. (Color on line) Sensitivity on launching position—orbit angle ω_0. (Right scales): FE_r (green triangles) and FE_{TOF} (blue circles) following deflection by π, i.e. evaluated at $\omega = \omega_0 + \pi$, are plotted as a function of the launching orbit angle ω_0. (Left scale) $FE_{\mathcal{E}_r}$ (red open squares) at launching position $\omega = \omega_0$ (identical to $FE_{\mathcal{E}_r}$ in Figs. 3 and 4, but blown up in the y-scale and covering the 0–180° range only). Results are for motion in the XY ($Z = 0$) plane and for the *principal* ray (orbit II) only, shown in Fig. 1, and geometries A, B and C. Variations in FE_r and FE_{TOF} at $\omega = \omega_0 + \pi$ are correlated to variations in $FE_{\mathcal{E}_r}$ at the launching point $\omega = \omega_0$. The launching point $\omega = 0°$ (see Fig. 1) used in all calculations presented in this paper, corresponds to $\omega_0 = 0°$.

are given on the right scale; thus, apart from the cumulative effect of integrating along the fixed path length, correlation with initial electric field values can be more evident. The values of FE_r and FE_{TOF} are seen to show some variation with ω_0 leading to a *further* overall maximum error of about ±10% around the mean position in the two FEs in all three geometries. The starting position dependent error for the principal ray orbit is listed in Table 6 of the summary as the additional ± error.

5.2. Elliptical orbits with $|\alpha| \le \alpha_{max}$, $r_0 = 101.6$ mm and $\rho = 0.5748$

So far we have only investigated circular orbits for which we always have $\alpha = 0°$. Here we compare radial FEs as a function of ω with $\alpha \neq 0°$. Non-zero α values are also needed in the generation of line shapes at $\omega = 180°$, the first-order HDA focus plane, and are therefore also included in this section.

5.2.1. $FE_r(\omega)$ for $r_0 = 101.6$ mm and $\alpha_{max} = 5°$

Trajectories with $\alpha \neq 0°$ are elliptical and therefore have a more varied distance from either electrode surface than the circular orbits already investigated. In Fig. 6, such FE_r's are presented, though only for trajectories with $r_0 = \bar{R}$. Again, geometry B is seen to give more accurate results than geometries A and C. In particular, $FE_r(\alpha, \omega)$, while dependent in general on α, is seen at $\omega = 180°$ to be relatively insensitive to α, whereas FEs for negative and positive α are seen to cross in geometry A and B, but not C, close to $\omega = 315°$. Overall, the α dependence, at least for rays starting from $r_0 = \bar{R}$, introduces only small additions to the $\alpha = 0°$ radial FEs, which at $\omega = 180°$ are practically negligible.

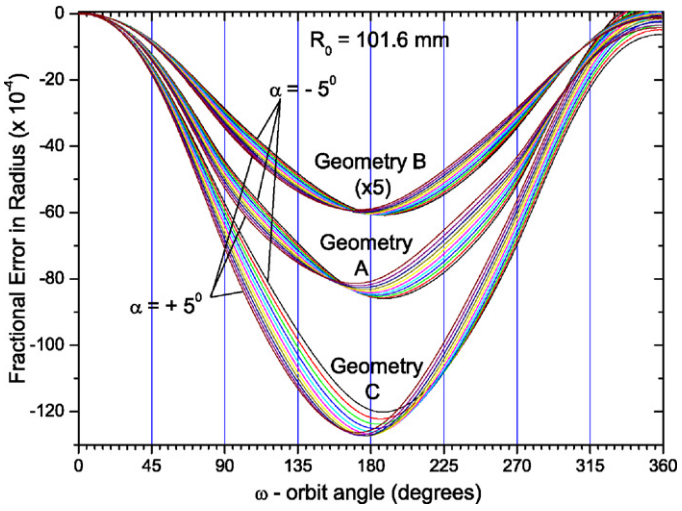

Fig. 6. (Color on line) Plots of the radial fractional error $FE_r(\alpha, \omega)$ as a function of ω for geometries A, B and C with fractional interradial electrode spacing $\rho = 0.5748$. The lines correspond to trajectories for $r_0 = \bar{R}$ and $|\alpha| \leq 5^\circ$ with an increment of 1°.

5.2.2. *Line shapes at $\omega = 180^\circ$ for a monoenergetic point source at $r_0 = 81.6$, 101.6, 121.6 mm and $\alpha_{max} = 2^\circ$*

Both the absolute and relative radial FE can be investigated at particular values of ω using Monte-Carlo techniques to generate line shapes. These line shape results are only relevant in accuracy evaluations of SIMION since they reflect some kind of cumulative error averaged over the number of trajectories used. Here, 100,000 electrons were flown with α randomly varied so that $|\alpha| \leq \alpha_{max} = 2^\circ$. Theoretical line shapes were computed at $\omega = 180^\circ$ using Eq. (6). Generation of line shapes at this deflection angle is particularly relevant for spectroscopy since it is here that HDA exit slits or position sensitive detectors are placed to take advantage of the first order focus point in α. SIMION generated line shapes are compared to theory for geometries A, B and C in Fig. 7.

The peak positions are pulled in towards smaller exit radii, with peak position FEs very close to those determined from $\alpha = 0^\circ$ trajectories evaluated at $\omega = 180^\circ$ (see Figs. 3 and 4) and in agreement also with observations for non-zero α values discussed in Section 5.2.1. The line shapes generated using geometry B were always found to be the closest both to theory (as was true of radial peak position), with geometry A coming in a close second. In geometry C, but only for the two outermost radii $r_0 = 81.6$ mm and $r_0 = 121.6$ mm, the line shapes are seen to have longer tails leading to increased base width and asymmetry. This reaffirms the increased sensitivity of the orbits closest to the electrode surfaces, especially at low grid density. Both $FE_r(\omega = \pi)$ and $FE_{bw}(\omega = \pi)$ as determined from the peak positions and base widths (bw) of the line shapes presented in Fig. 7 are listed in Table 6 with $FE_{bw} = (bw_{sim} - bw_{theory})/bw_{theory}$.

We note that for the three r_0 cases considered, only $r_0 = \bar{R} = 101.6$ mm (Fig. 7 middle) really corresponds to a typical electron spectroscopy application (with the SC replaced by an HDA). The other two cases, $r_0 = 81.6$ mm and $r_0 = 121.6$ mm, are unnatural for spectroscopy applications since the field in the SC is set by a principal ray ($R_0 = R_\pi = \bar{R} = 101.6$ mm and w = 1000 eV) far removed from the ray pencils flown generating the line shapes.

5.3. *ρ-dependence of FEs for principal ray*

We next investigate the dependence of the FEs on the SC fractional interradial electrode spacing $\rho = \Delta R/\bar{R}$ for fixed $\bar{R} = 101.6$ mm. We examine only the principal ray for five different values of ρ (given in Table 4) in the range $\rho = 0.18$–0.97. Similar dependencies are seen in all three geometries as exemplified by the results for geometry A shown in Fig. 8. For all FEs, the FE increases with decreasing value of ρ, consistent with the picture that the closer the electrode surfaces come to the orbit the bigger the effect of the surface errors on the trajectory and therefore the larger the differences between simulation and theory. Though not shown, the FEs of geometry A and C were found to be very similar and always larger in magnitude by a factor of ~10 than the FEs of geometry B, and the kinetic energy FEs were larger by a factor of ~200. These results are consistent with what was already found for $\rho = 0.5748$ at the other two radii $r_0 = 81.6$ mm and $r_0 = 121.6$ mm shown in Figs. 3 and 4.

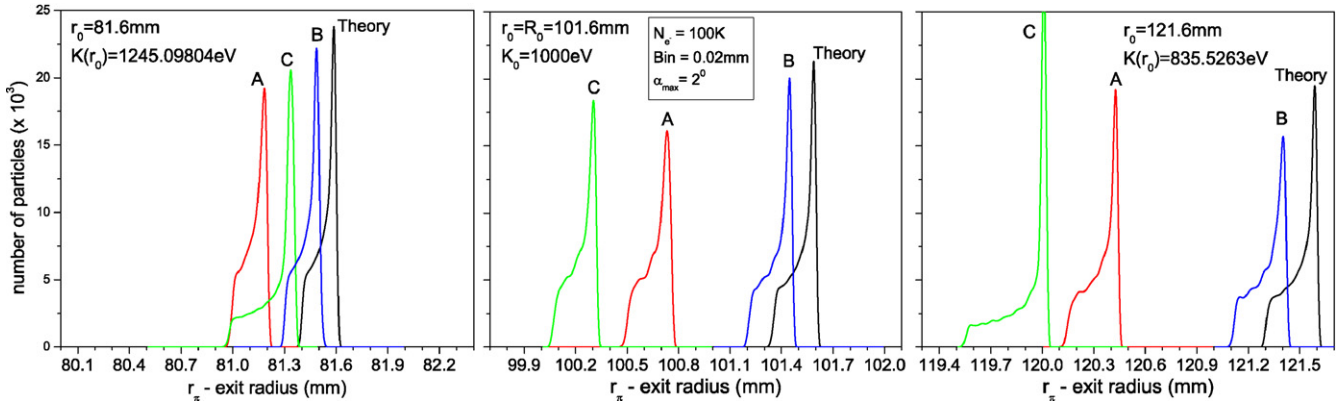

Fig. 7. (Color on line) Comparison of line shapes generated by "flying" 100,000 electrons from a point source at radii $r_0 = 81.6$ mm (left), $r_0 = 101.6$ mm (middle) and $r_0 = 121.6$ mm (right) with random entry angles $|\alpha| \leq \alpha_{max} = 2^\circ$. In each case, the launching kinetic energy $K(r_0)$ is indicated. The same set of random α-values was used in the generation of each line shape: theory (Eq. (6)) and A, B and C corresponding to the respective SIMION geometries (Table 3). A bin size of 0.02 mm was used for averaging. For all three r_0 values the geometry with the highest grid density ($\lambda = 10$ gu/mm – B) is seen to come closest to theory in both shape and position.

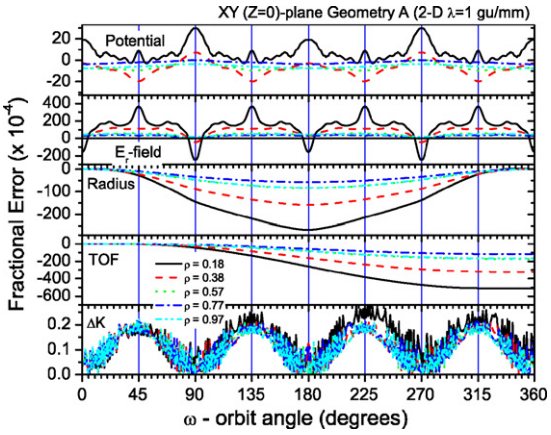

Fig. 8. (Color on line) Same as Fig. 3 (geometry A), but for different fractional interradial electrode spacings $\rho = \Delta R/\bar{R}$ and with fixed $\bar{R} = 101.6$ mm for all values of ρ. Lines: $\rho = 0.1811$ (continuous—black), $\rho = 0.3779$ (dash—red), $\rho = 0.5748$ (dot—green), $\rho = 0.7717$ (dash-dot—blue), $\rho = 0.9685$ (dash-dot-dot—azure).

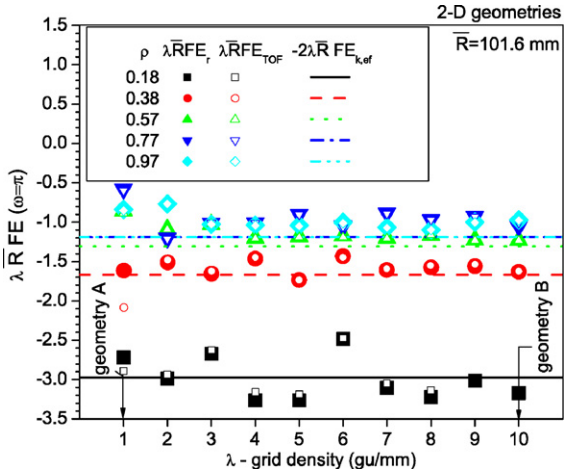

Fig. 9. (Color on line) Data points: $\lambda\,\bar{R}\,\mathrm{FE_r}$ (closed symbols) and $\lambda\,\bar{R}\,\mathrm{FE_{TOF}}$ (open symbols) for principal ray (circular orbits with $r_0 = \bar{R} = 101.6$ mm and $\alpha = 0°$) in 2-D geometries at $\omega = \pi$. Lines: theoretical empirical fit (ef) model shown in Fig. 12.

5.4. λ and ρ-dependence of radius and TOF FEs for principal ray at ω = 180°

Finally, we explore both λ and ρ-dependence of the radius and TOF FEs for the principal ray at the first order focus plane ($\omega = 180°$). The data were generated at the five different values of ρ, already shown in Fig. 8 for geometry A, each at electrode densities λ = 1–10 gu/mm in increments of $\Delta\lambda = 1$. Thus, the entire geometry space between geometry A (λ = 1) and B (λ = 10) is covered. In Fig. 9, both FEs are shown as a function of λ for each of the five values of ρ. The lines correspond to the theoretical model which is described in the next section. The most striking feature is the clear $1/\lambda$ dependence of both FEs, in agreement with expectations. Also, as observed previously, both radius and TOF FEs are found to be roughly equal at $\omega = 180°$ for the same λ and ρ.

6. Theoretical model for $\mathrm{FE_r}$ and $\mathrm{FE_{TOF}}$

The fractional errors were presented and characterized in the previous section. We now proceed to develop a theoretical model to predict these errors more generally. The approach will follow what we have already observed: that the small modeling errors in the simulated electrode radii, $d_{i,j}$, will induce slight inaccuracies in the field ($\mathrm{FE_V}$ and $\mathrm{FE}_{\mathcal{E}_r}$), which will in turn perturb the particle from its theoretical trajectory ($\mathrm{FE_r}$ and $\mathrm{FE_{TOF}}$).

6.1. Basic assumptions concerning the field error

In building the theoretical model, we shall assume the following to be true:

$$(1-\mathrm{a}) \quad \tilde{V}_{\mathrm{sim}}(r) \approx \tilde{V}(k_{\mathrm{sim}}, c_{\mathrm{sim}}, r) = \tilde{V}(k, c, r) + \Delta\tilde{V} \tag{27}$$

$$(1-\mathrm{b}) \quad \mathcal{E}_{\mathrm{r\,sim}}(r) \approx \mathcal{E}_{\mathrm{r}}(k_{\mathrm{sim}}, r) = \mathcal{E}_{\mathrm{r}}(k, r) + \Delta\mathcal{E}_{\mathrm{r}} \tag{28}$$

$$(2-\mathrm{a}) \quad k_{\mathrm{sim}} = k(R_{1\mathrm{sim}}, R_{2\mathrm{sim}}) \tag{29}$$

$$\approx k(R_1 + \Delta R_1, R_2 + \Delta R_2) = k + \Delta k \tag{30}$$

$$(2-\mathrm{b}) \quad c_{\mathrm{sim}} = c(R_{1\mathrm{sim}}, R_{2\mathrm{sim}}) \tag{31}$$

$$\approx c(R_1 + \Delta R_1, R_2 + \Delta R_2) = c + \Delta c \tag{32}$$

These assumptions naturally lead to the following corollaries concerning the trajectory errors:

$$\Delta k \text{ and } \Delta c \text{ are } r\text{- and } \omega\text{-independent} \tag{33}$$

$$r_{\mathrm{sim}}(\omega, k_{\mathrm{sim}}) \approx r_\omega(k + \Delta k) = r_\omega + \Delta r_\omega \tag{34}$$

$$T_{\mathrm{sim}}(\omega, k_{\mathrm{sim}}) \approx T_\omega(k + \Delta k) = T_\omega + \Delta T_\omega \tag{35}$$

Assumption (1) requires that the SIMION potential V_{sim} (and its derivative the electric field $\mathcal{E}_{\mathrm{r\,sim}}$) be modeled by the ideal potential/field Eqs. (1) and (2), but with constants k and c replaced by the new, slightly different constants k_{sim} and c_{sim}.

Assumption (2) gives the values of the field constants k_{sim} and c_{sim} in terms of the errors Δk and Δc. Furthermore, Δk and Δc are directly related to the modeling errors, ΔR_1 and ΔR_2, on the electrode surfaces via Eqs. (4) and (5).

Corollary Eq. (33) is just a statement of the constancy of the field and potential errors Δk and Δc. In particular, it requires for simplicity that k_{sim} (and c_{sim}) be both r- and *ω-independent*, at least to first order. With the ω-independent assumption, the field perturbation has a simple form that can be applied directly to the *final* trajectory equations (Eqs. (6) and (7)), which remains analytic. An ω-dependent perturbation would need to be implemented *prior* to solving the equations of motion and would make the trajectory determination more complex and probably amenable only to a numerical treatment. We note that since only k enters the equation of motion, we shall not be interested anymore in c. It is useful to define FE_k as:

$$\mathrm{FE}_k \equiv \frac{k_{\mathrm{sim}} - k}{k} = \frac{\Delta k}{k} \tag{36}$$

Table 4
Values of radii and voltages for the SC of Table 1 for five fractional interradial electrode spacings $\rho = \Delta R/\bar{R}$

ρ	0.181102	0.377953	0.574803	0.771654	0.968504
R_1	92.40	82.40	72.40	62.40	52.40
R_2	110.80	120.80	130.80	140.80	150.80
ΔR	18.4	38.4	58.4	78.4	98.4
$\tilde{V}_1$	199.1342	466.0194	806.6298	1256.4103	1877.8626
$\tilde{V}_2$	−166.0650	−317.8808	−446.4832	−556.8182	−652.5199
$\Delta\tilde{V}$	−365.1992	−783.9002	−1253.1130	−1813.2284	−2530.3825

Radii are in (mm) and voltages in (V).

Then, according to assumption (1-b), in the limit that the SIMION field $\mathcal{E}_{\mathrm{r\,sim}}(r)$ approaches the ideal model field $\mathcal{E}_{\mathrm{r}}(k_{\mathrm{sim}}, r)$:

$$\mathcal{E}_{\mathrm{r\,sim}}(r) \approx \mathcal{E}_{\mathrm{r}}(k_{\mathrm{sim}}, r) = -k_{\mathrm{sim}}/r^2 \tag{37}$$

we should have the equality:

$$\mathrm{FE}_k = \mathrm{FE}_{\mathcal{E}_{\mathrm{r}}} \tag{38}$$

In Fig. 10 (top), $\mathrm{FE}_{\mathcal{E}_{\mathrm{r}}}$ is plotted against the radius $r\,(R_1 \le r \le R_2)$ in geometries A, B, and C. At each r the $\mathrm{FE}_{\mathcal{E}_{\mathrm{r}}}$ values are averaged over all ω (typical trajectory) for clarity. We see that $\mathrm{FE}_{\mathcal{E}_{\mathrm{r}}}$ is approximately constant only in a central region away from the surfaces, so the ideal $1/r$ field assumption holds only in this central region. However, the size of this region increases with increasing λ (geometry B). Also shown in the same plots are the values of FE_k that model $\mathrm{FE}_{\mathcal{E}_{\mathrm{r}}}$, evaluated at three different values of constant k_{sim} obtained by the corresponding model calculation described in Section 6.3.

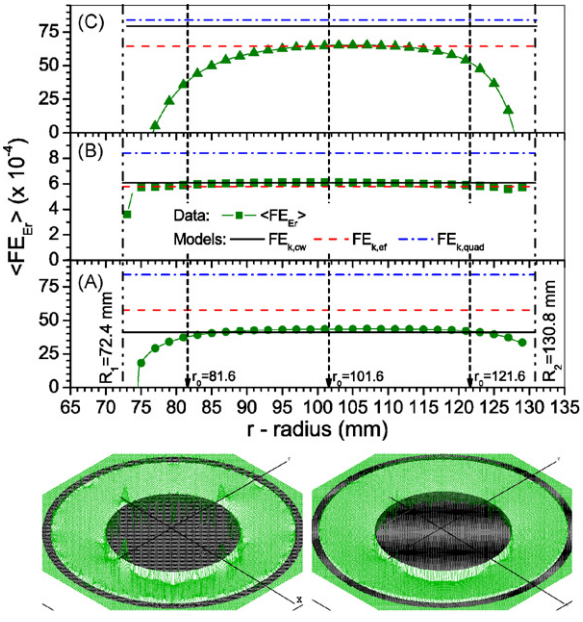

Fig. 10. (Color on line) (Top) Averaged measured $\mathrm{FE}_{\mathcal{E}_{\mathrm{r}}}$ over ω at each radius r for geometries A, B, and C with corresponding labeled panels. Values are roughly constant over the central region as assumed by the models also shown for comparison. The positions of r_0 at which the FEs of Figs. 3 and 4 were evaluated are indicated by the arrows. (Bottom) The difference between the simulated and exact theoretical potentials (which is proportional to $\mathrm{FE_V}$) is plotted over the full XY $(Z = 0)$ orbit plane of electron motion for geometry A (bottom left) and B (bottom right). Geometry C (not shown) appears somewhat similar to A.

Without the averaging over ω above, the individual $\mathrm{FE}_{\mathcal{E}_{\mathrm{r}}}$ values in the central region vary with a standard deviation of about 20% (in B and C) or 50% (in A) across ω, as already observed in Figs. 3 and 4. Clearly, Δk (and Δc) are therefore to some extent ω-dependent, contrary to corollary Eq. (33). Varying amounts of ω-dependence were also seen in the related $\mathrm{FE}_{\mathcal{E}_{\mathrm{r}}}$ values in Figs. 3 and 4. However, the ω-dependence is less significant than that of the underlying modeling errors, $d_{i,j}$, shown in Fig. 2 (bottom) due to the averaging effect of the finite difference method, particularly away from the surfaces. The ω-independence assumption is also justified on the grounds that the trajectories we are concerned with traverse a range of ω, thereby averaging out much of the remaining effect of the local deviations as the regular behavior of Fig. 10 (top) suggests.

Fig. 10 (bottom) offers a more global perspective. The difference between the simulated and exact theoretical potentials, which is proportional to $\mathrm{FE_V}$, is plotted over the full XY $(Z = 0)$ orbit plane of electron motion. (This is a SIMION PE plot of a PA having potentials set by PERL script `sc_make_verror_pa.pl` to this difference.) The sudden peaks and sharp precipices indicated, particularly close to the inner electrode surface ought to have a strong effect on orbits closest to these perturbations. These structures are repeated periodically with ω having a clear correspondence with structures already observed in the $\mathrm{FE_V}(\omega)$ of Figs. 3 and 4. The surface in geometry B is much more smooth as expected for higher grid density. Thus, we expect the assumptions to be more valid for geometry B than for geometries A and C and to better extend over non-central trajectories I and III, as already discussed. In particular, note the prominent and approximately constant precipices near the inner and outer electrode surfaces. These correspond to non-zero surface error constants ΔR_i mentioned in Assumption (2). The directions and magnitudes of these precipices indicate an overall positive and roughly constant value of $\mathrm{FE}_{\mathcal{E}_{\mathrm{r}}}$ (or FE_k) as already noted.

6.2. *Relating trajectory errors* $\mathrm{FE_r}$ *and* $\mathrm{FE_{TOF}}$ *to field errors* Δk*, with* ω*-dependence*

Assumptions (1) and (2) then naturally lead to the corollary expressed in Eqs. (34) and (35) requiring that $r_{\mathrm{sim}}(\omega)$ and $T_{\mathrm{sim}}(\omega)$ maintain the same theoretical form as r_ω and T_ω (see Eqs. (6) and (7)) but with k replaced by $k_{\mathrm{sim}} = k + \Delta k$. We may then expand both $r_\omega(k + \Delta k)$ and $T_\omega(k + \Delta k)$ to first order in Δk to obtain expressions for $\mathrm{FE_{TOF}}$ and $\mathrm{FE_r}$ in terms of FE_k according to the theoretical model:

$$\mathrm{FE_r}(\omega) = \frac{r_\omega(k+\Delta k) - r_\omega(k)}{r_\omega(k)} \approx -2\,\mathrm{FE}_k \times \frac{(1-\cos\omega)}{[2-(1-\eta)\,\cos\omega + (1+\eta)\,\cos(2\,\alpha+\omega)]} \tag{39}$$

$$\mathrm{FE_{TOF}}(\omega) = \frac{T_\omega(k+\Delta k) - T_\omega(k)}{T_\pi(k)} \approx -2\,\mathrm{FE}_k \left[1 + (1+\eta)\,\frac{\partial_\eta I(\eta,\alpha,\omega)}{2\,I(\eta,\alpha,\omega)}\right] \tag{40}$$

Both Eqs. (39) and (40) depend on the parameter η rather than on each of r_0 and $K(r_0)$, independently. Thus, since for all circular orbits $\eta = 0$, both theoretical FEs are independent of r_0 (and $K(r_0)$) as expected from our discussion above. The integrals in Eq. (40) can be analytically evaluated for circular orbits ($\eta = 0$, $\alpha = 0^\circ$) in which case we have:

$$\mathrm{FE_r}(\omega) \approx -2\,\mathrm{FE}_k \frac{(1-\cos\omega)}{2} \tag{41}$$

$$\mathrm{FE_{TOF}}(\omega) \approx -2\,\mathrm{FE}_k \frac{(\omega - \sin\omega)}{\pi} \tag{42}$$

Note that the two FEs are closely related by a derivative, and at the focal plane, $\omega = 180^\circ$, we have this interesting equality:

$$\mathrm{FE_r}(\omega=\pi) \approx \mathrm{FE_{TOF}}(\omega=\pi) \approx -2\,\mathrm{FE}_k \tag{43}$$

already observed in Figs. 3, 4, 8 and 9. We note that the negative $\mathrm{FE_r}$ generally observed in Figs. 3 and 4 is therefore implied by the positive FE_k in the fairly broad region around the mean radius shown in Fig. 10 (top).

We shall limit our investigation to nominally circular orbits $\eta = 0$ with $\alpha = 0$, even though it is very likely that Eqs. (41) and (42) still apply for $\eta \neq 0$. For $\alpha \neq 0$ we have already seen that the variation in the radial FEs is very small particularly at the focal plane of interest here. Thus, it should be possible to use our theoretical FEs for circular orbits to also predict the FEs for non-circular orbits.

6.3. *Estimating field error* FE_k *from modeling errors* d_i

We now are left with the final task of determining a procedure for evaluating the overall scaling parameter FE_k required in Eqs. (41) and (42). We would ultimately like to do so directly from the SIMION electrode modeling errors $d_{i,j}$ ($i = 1, 2$) mentioned in Section 3. Using the definition of FE_k Eq. (36) we have:

$$\mathrm{FE}_k = \frac{k(R_{1\mathrm{sim}}, R_{2\mathrm{sim}}) - k(R_1, R_2)}{k(R_1, R_2)} \tag{44}$$

$$\approx \frac{(\Delta R_1 \frac{R_2}{R_1} - \Delta R_2 \frac{R_1}{R_2})}{\Delta R} \tag{45}$$

where Eq. (45) results if we replace $R_{i\,\mathrm{sim}}$ with $R_i + \Delta R_i$ and keep only terms to first order in ΔR_i in the spirit of the first order perturbation theory assumption expressed in Eq. (30).

We may define surface error d_i in grid units (gu) such that $d_i \equiv \Delta R_i\,\lambda$ for $i = 1, 2$. Then using Eqs. (A.18) and (A.19), expressing R_i in terms of ρ for fixed $\bar{R}$, and replacing R_i and ΔR_i in Eq. (45), we obtain a new ρ-dependent expression for FE_k:

$$\mathrm{FE}_k = \frac{-d_1 + d_2\,\chi(\rho)}{-2\,\lambda\,\bar{R}\,F(\rho)} \tag{46}$$

with $F(\rho)$ and $\chi(\rho)$ defined as:

$$F(\rho) \equiv \left(\frac{\rho}{2}\right)\left(\frac{2-\rho}{2+\rho}\right) \tag{47}$$

$$\chi(\rho) \equiv \left(\frac{2-\rho}{2+\rho}\right)^2 \tag{48}$$

As observed in Fig. 9, FE_k is expected to scale inversely with the product $\lambda\,\bar{R}$.

For FE_k to be independent of ω (see condition in Eq. (33)) d_1 and d_2 must also be independent of ω, even though they depend locally on λ and ρ. As a first approximation we shall assume that d_1 and d_2 are just *constant* parameters that can be determined empirically by fitting or, as is the focus of the remainder of this paper, predicted from the individual $d_{i,j}$ values. The trajectory FEs according to Eq. (43) will then be given by:

$$\mathrm{FE_r}(\omega=\pi) = \mathrm{FE_{TOF}}(\omega=\pi) = \frac{-d_1 + d_2\,\chi(\rho)}{\lambda\,\bar{R}\,F(\rho)} \tag{49}$$

We note that the values of d_1 and d_2 can also be experimentally"measured" in SIMION as follows. We first solve for k_{sim} and c_{sim} constants using the defining equations Eqs. (1) and (2):

$$k_{\mathrm{sim}} = -\mathcal{E}_{\mathrm{r\,sim}}(r_{\mathrm{sim}})\,r_{\mathrm{sim}}^2 \tag{50}$$

$$c_{\mathrm{sim}} = \tilde{V}_{\mathrm{sim}}(r_{\mathrm{sim}}) + k_{\mathrm{sim}}/r_{\mathrm{sim}} \tag{51}$$

where the actual SIMION potential V_{sim} and field $\mathcal{E}_{\mathrm{r,sim}}$ are "measured" at radius r_{sim}. Then using these values in Eq. (1) we can obtain values $R_{i\,\mathrm{sim}}$ and d_i for $i = 1, 2$:

$$R_{i\,\mathrm{sim}} = \langle k_{\mathrm{sim}}\rangle / (\langle c_{\mathrm{sim}}\rangle - \tilde{V}_i) \tag{52}$$

$$d_i = (R_{i,\mathrm{sim}} - R_i)\lambda \tag{53}$$

Finally, the ω-averaged values $\langle R_{i\,\mathrm{sim}}\rangle$, $\langle d_i\rangle$ and $\langle \mathrm{FE}_k\rangle$ are computed and listed in Table 5 (rows labeled SIMION) for comparison with the model results. The entire procedure has been implemented in our PERL script `sc_measure_kc.pl`.

6.3.1. *Quadrature error propagation model—*$\mathrm{FE}_{k,quad}$

To impose some bounds on the FEs above, we might assume to a rough approximation that the individual modeling errors $d_{i,j}$ over the surface (Fig. 2 bottom) operate independently and can be added in quadrature according to the propagation of errors formulation:

$$\Delta k = \sqrt{(\partial k/\partial d_1)^2 d_1^2 + (\partial k/\partial d_2)^2 d_2^2} \tag{54}$$

The d_i values here are taken as the standard deviations over the surface of the individual $d_{i,j}$ values in Fig. 2 (bottom). We find that for all geometries studied (both 2-D and 3-D), the individual $d_{i,j}$ are in the range $[-0.5, +0.5]$ gu with standard deviations d_i fairly consistent at 0.26 ± 0.1 gu (this is just under

Table 5
Comparison of the FEs predicted by the various theoretical models to the FEs observed in SIMION

Model	Geometry	λ (gu/mm)	d_1 (gu)	d_2 (gu)	FE_k ($\times 10^{-4}$)	FE_r or FE_{TOF} ($\times 10^{-4}$)
SIMION	A(2-D)	1	0.1112[a]	−0.0954[a]	43.598[a]	−84.3/ − 87.2[a]
quad	A(2-D)	1	±0.260	±0.260	84.123	−168.25
ef	A(2-D)	1	0.13203 ± 0.00628	−0.17890 ± 0.01525	57.797	−115.59
nw	A(2-D)	1	0.00168	0.001804	0.34859	−0.69717
sw	A(2-D)	1	0.1077	−0.0961	42.438	−84.876
cw	A(2-D)	1	0.1039	−0.0946	41.102	−82.205
SIMION	B(2-D)	10	0.1542[a]	−0.1413[a]	6.1130[a]	−12.1/ − 12.1[a]
quad	B(2-D)	10	±0.260	±0.260	8.4123	−16.825
ef	B(2-D)	10	0.13203 ± 0.00628	−0.17890 ± 0.01525	5.7797	−11.559
nw	B(2-D)	10	0.0619	−0.0459	2.3519	−4.7048
sw	B(2-D)	10	0.1570	−0.1425	6.2079	−12.416
cw	B(2-D)	10	0.1539	−0.1396	6.0852	−12.170
SIMION	2-D	100	0.0907[ab]	−0.1000[ab]	0.3753[ab]	−0.7569/ − 0.7078[ab]
quad	2-D	100	±0.260	±0.260	0.84123	−1.6825
ef	2-D	100	0.13203 ± 0.00628	−0.17890 ± 0.01525	0.57797	−1.1559
nw	2-D	100	0.0493	−0.0441	0.19420	−0.38840
sw	2-D	100	0.1440	−0.1399	0.57791	−1.1558
cw	2-D	100	0.1412	−0.1369	0.56649	−1.1330
SIMION	C(3-D)	1	0.1617[a]	−0.1551[a]	65.055[a]	−126.8/ − 125.6[a]
quad	C(3-D)	1	±0.260	±0.260	84.123	−168.25
ef	C(3-D)	1	0.19552 ± 0.00490	−0.04213 ± 0.01190	64.478	−128.96
nw	C(3-D)	1	0.0765	−0.0768	30.935	−61.870
sw	C(3-D)	1	0.1892	−0.1918	76.701	−153.40
cw	C(3-D)	1	0.1973	−0.1953	79.531	−159.06
SIMION	3-D	4	0.1716[ab]	−0.1584[ab]	17.05[ab]	−33.76/ − 33.43[ab]
quad	3-D	4	±0.260	±0.260	21.031	−42.06
ef	3-D	4	0.1955	−0.0421	16.120	−32.239
nw	3-D	4	0.0817	−0.0777	8.1600	−16.320
sw	3-D	4	0.1961	−0.1919	19.714	−39.428
cw	3-D	4	0.2013	−0.1957	20.207	−40.414
Prediction for $\rho = 0.25$, $\bar{R} = 50$ mm ($R_1 = 43.75$ mm, $R_2 = 56.25$ mm), $\lambda = 5$ in a 2-D geometry						
SIMION	2-D	5	0.1613[a]	−0.1445[a]	51.441[a]	−104.14/ − 100.88[a]
quad	2-D	5	±0.260	±0.260	62.511	−125.02
ef	2-D	5	0.13203 ± 0.00628	−0.17890 ± 0.01525	49.422	−98.843
nw	2-D	5	0.0737	−0.0573	22.292	−44.585
sw	2-D	5	0.1689	−0.1516	53.620	−107.24
cw	2-D	5	0.1675	−0.1489	52.993	−105.99

The theoretical models (quad, quadrature; ef, empirical fit; nw, non-weighting; sw, simple weighting; cw, complex weighting) are described in Section 6. FE_k, d_1, and d_2 are obtained from the models and compared to corresponding values obtained from measuring the SIMION average field along r ($FE_{\mathcal{E}_r}$ and FE_V and Eqs. (38) and (53)). Values of FE_r and FE_{TOF} "experimentally" determined from SIMION trajectories and compared to corresponding values predicted from the model using $FE_r \approx FE_{TOF} \approx -2\,FE_k$ (Eq. (43)). SIMION results were determined only for the central orbit $r = r_0 = \bar{R} = 101.6$ mm, with trajectory FEs obtained at $\omega = \pi$. SC uses $R_1 = 72.4$ mm and $R_2 = 130.8$ mm ($\bar{R} = 101.6$ mm, $\rho = 0.574803$), but the last example examines the special case of $\rho = 0.25$, $\bar{R} = 50$ mm $\lambda = 5$ in a 2-D geometry. The limiting case with $\lambda = 100$ gu/mm is also given for the 2-D geometry as a special application. The values of d_i, FE_k and FE_r in the various models can be readily calculated at our special web site model calculator [35].

[a] "Experimentally" determined values.
[b] Used SIMION 8 with 2GB RAM.

∼0.29, which is the standard deviation expected if the numbers in this range [−0.5, +0.5] gu were uniformly random).

Using the expression for k given by Eq. (5) and evaluating the partial derivatives then leads to the result

$$FE_{k,\mathrm{quad}} = \frac{\sqrt{d_1^2 + d_2^2\,\chi(\rho)^2}}{2\,\lambda\,\bar{R}\,F(\rho)} \tag{55}$$

which of course is by definition positive and therefore cannot predict the sign of the error. The value $\pm FE_{k,\mathrm{quad}}$, thus establishes a rough (and likely non-minimal) bounds estimate on FE_k. It may similarly be substituted into the other FE formulas.

SIMION FEs for a sampling of geometries are listed in Table 5 and are seen to be within the predicted estimated bounds of $FE_{k,\mathrm{quad}}$. In Fig. 11 these FEs are plotted over ω.

6.3.2. Empirical fit model—$FE_{k,ef}$

Having suggested that d_1 and d_2 are likely within the range ±0.26 gu, we now empirically obtain more precise values for them. This is done by fitting to our $FE_r(\omega = \pi)$ data scaled in both the x- and y-axis by the functions $\chi(\rho)$ and $F(\rho)$, respectively, as shown in Fig. 12. With the above definitions a simple linear fitting of the d_i constants is possible. The spread in the 2-D data at each ρ value (bottom) is due to the various values of

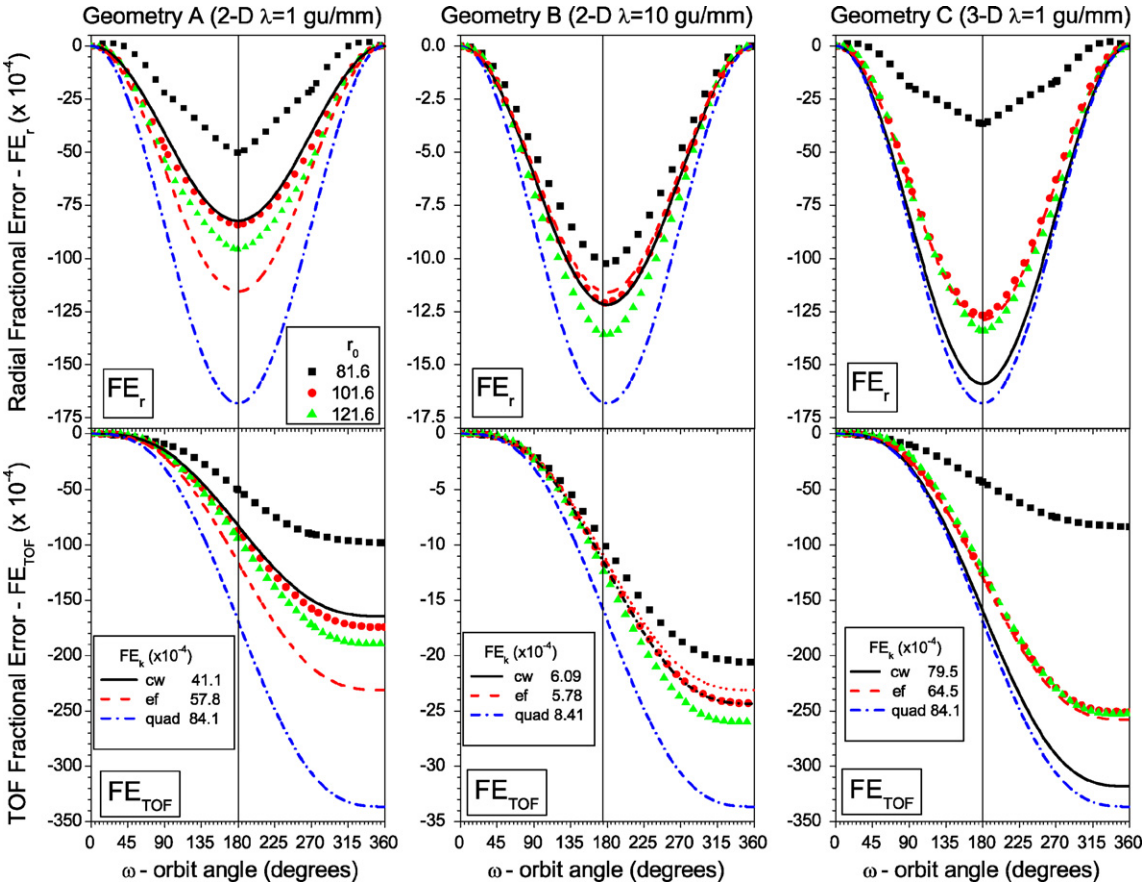

Fig. 11. (Color on line) Comparison of theoretical models cw, ef and quad based on Eqs. (41) and (42) with the radial (top row) and TOF (bottom row) FEs of circular orbits I ($r_0 = 81.6$ mm), II ($r_0 = 101.6$ mm) and III ($r_0 = 121.6$ mm) as a function of ω for geometries A (left), B (middle) and C (right). Best agreement is seen for cw model with orbit II in geometries A and B. Theoretical models are not r_0-dependent.

λ at which these were obtained. For 3-D geometries only $\lambda = 1$ data were obtained since much larger values ($\lambda > 2$) would lead to SIMION PAs with prohibitively large memory requirements (see Table 3).

The two-parameter fit clearly does a reasonable job overall. Both d_1 and d_2 are within the 0 ± 0.26 gu in agreement with previous expectations. d_1 is seen to be positive and d_2 to be negative showing that the two surfaces effectively extend *outward* into space by a small fraction of a grid unit: $R_{1\text{sim}} = R_1 + d_1/\lambda$ mm, $R_{2\text{sim}} = R_2 + d_2/\lambda$ mm, with d_1 and d_2 given in grid units in the legend of Fig. 12. This is consistent with the observations in Section 5.1.1.

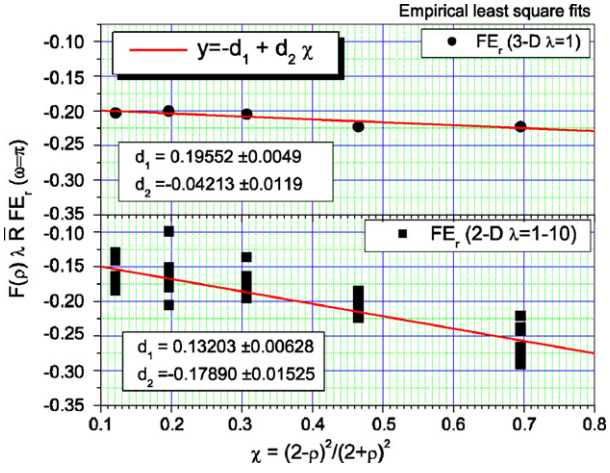

Fig. 12. (Color on line) Least-square-fit of two-parameter empirical fit model (ef) (see Eq. (49)) to the rescaled data for $\text{FE}_\text{r}(\omega = \pi)$ shown in Fig. 9 for both 2-D geometries (bottom) and 3-D geometry C (top). The resulting effective thicknesses d_i are given in the legends with their fitting errors.

6.3.3. Simple average model—$FE_{k,nw}$

To explain the empirical values of d_i computed above from the modeling errors $d_{i,j}$ in Fig. 2 (bottom), one might readily attempt to compute the mean values of the $d_{i,j}$ and substitute those means for the d_i constants in Eq. (46):

$$\text{FE}_{k,\text{nw}} = \frac{-\langle d_{1,j}\rangle + \langle d_{2,j}\rangle\, \chi(\rho)}{-2\,\lambda\,\bar{R}\,F(\rho)} \tag{56}$$

The "nw" stands for "non-weighted" and is meant to distinguish it from the "weighted" mean used later. 2-D results are averaged over the circumference of a circle (in the XY plane), while 3-D results are averaged over the surface of a sphere.

Results are shown in Table 5 as before. Typically, the 3-D averages are larger (and less variant) due to extra contributions from non-XY plane values. Most importantly, the errors computed here are a fraction of the errors in the SIMION data. Obviously, there must be a more important factor contributing to the error.

6.3.4. Weighted average models—$FE_{k,sw}$ and $FE_{k,cw}$

Instead of taking the simple average of the modeling errors $d_{i,j}$, as done previously, a much better estimate of surface error is obtained by using a *weighted average* of these values, with weights defined by point topology. Qualitatively, the surface points that are sharpest on the exterior or are on sections that are longest should have higher weights as they contribute most to the field (think of the SC spheres being replaced with spiked spheres).

Thus, assigning to each grid point j and point type t_j a corresponding weight $W(t_j)$, the weighted average leads to the expression:

$$\mathrm{FE}_{k,\mathrm{w}} = \frac{-\langle d_{1,j}\rangle_W + \langle d_{2,j}\rangle_W\, \chi(\rho)}{-2\,\lambda\,\bar{R}\,F(\rho)} \tag{57}$$

with the weighted averages defined as:

$$\langle d_{i,j}\rangle_W = \frac{\sum_{j=1}^{N} d_{i,j} W_{\mathrm{s}}(t_j)}{\sum_{j=1}^{N} W_{\mathrm{s}}(t_j)} \qquad (i = 1, 2) \tag{58}$$

Our topological classification of surface points for the 2-D case is shown in Fig. 13. Points are classified by the number of adjacent orthogonal and diagonal non-electrode points. The optimal weights used on the average can be found empirically by fitting them to SIMION data, either to SC systems or even to more basic parallel plate systems as done here. The following weights were used: Type 1: 1, type 2: 1, type 3: 1.57, type 4: 2.78. We note that types 1 and 2 are about identical, while type 4 is the sharpest, so as expected it has the highest weight. Type 3 actually is not sharp at all; A straight 45° line contains all type 3 points and the field near it can be observed to be very accurate. The reason for the 1.57 weight probably has to do with the fact that the length of a type 3 point roughly corresponds to the length of the diagonal in a 1×1 square, which is $\sqrt{2}$, compared to length 1 for types 1 and 2. A similar analysis has also been carried out in 3-D, but involves a much more complex classification of points [34], beyond the scope of the present article.

We have found that this point classification scheme can be much simplified (especially in 3-D) while still producing good results for the SC. Points may be classified solely by orthogonal surface count: points with surface count 1 are weighted by 1, while points with a greater-than-one surface count are weighted by 3 (for 2-D geometries) or 5 (for 3-D geometries). This weighted average is crude, but useful. The two versions of the weighted average model are referred to as complex weighting (cw) and simple weighting (sw), respectively – $\mathrm{FE}_{k,\mathrm{cw}}$ and $\mathrm{FE}_{k_{\mathrm{sw}}}$.

Results are shown in Table 5 and for model cw in Fig. 11 as before. Predictions of $\mathrm{FE_r}$ and $\mathrm{FE_{TOF}}$ using the $\mathrm{FE}_{k,\mathrm{cw}}$ and $\mathrm{FE}_{k_{\mathrm{sw}}}$ values are shown to be in excellent agreement to the 2-D SIMION data at $r_0 = \bar{R}$. The model does over predict the 3-D data slightly because no attempt was made to take into account which plane the particles fly in (trajectories at an angle of 45° off the XY plane are found to have a bit higher FEs).

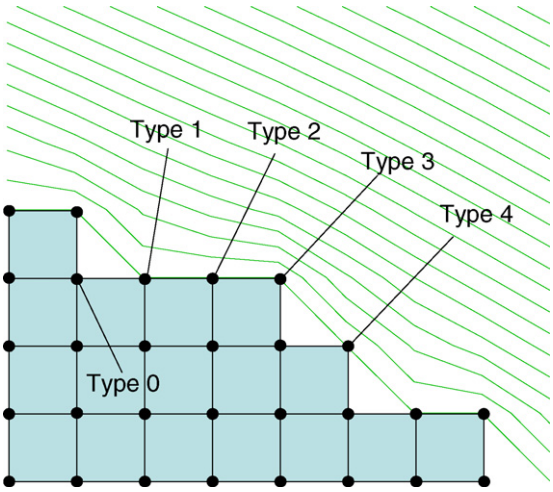

Fig. 13. (Color on line) Point type classification used in the complex weighted average model (2-D case). Each surface point contributes to the surrounding electric field differently depending on how well it is screened by its neighbors. Point type 0 is an internal point and has zero contribution. Equipotentials are shown in green.

6.3.5. Discussion

Using the formulas developed here we can predict the trajectory (radius and TOF) FEs at $\omega = \pi$ for any HDA. Such an example is listed in Table 5 for an HDA using a 2-D electrode geometry with a grid density $\lambda = 5$ gu/mm, a mean radius $\bar{R} = 50$ mm and $\rho = 0.25$. The three types of theoretical models (quadrature, empirical fit, and weighted average) are seen to give fairly good agreement with the measured SIMION results.

Estimation of the trajectory FE not only provides a measure of the error, but also the possibility to compensate for it. We found in general that for spherical surfaces a correction of $d_1 \approx -d_2 \approx 0.1$–$0.2$ gu in the radii is warranted electrostatically in SIMION version 7. For example, if in geometry A for $r_0 = 101.6$ mm we instead use $R_1 = 72.4 - 0.1 = 72.3$ gu and $R_2 = 130.8 - 1 + 0.1 = 129.9$ gu in the SIMION geometry file, we obtain a SIMION $\mathrm{FE_r} = 12.4 \times 10^{-4}$, which is much smaller in magnitude than the $\mathrm{FE_r} = -84.3 \times 10^{-4}$ obtained using the nominal values of $R_1 = 72.4$ mm and $R_2 = 130.8$ mm (see Table 5), in agreement with our analysis.

Also, by having a model for the error as a function of λ (e.g. $\mathrm{FE} \propto 1/\lambda$), we might simulate the system at various low values of λ and extrapolate those results to $\lambda = \infty$ (near perfect accuracy) [2]. The 2-D case with $\rho = 0.574803$ and $\lambda = 100$ gu/mm and 3-D case with $\lambda = 4$ represent a special application of the new SIMION version 8 with its expanded capabilities to handle much larger size PAs (in this case just under 2GB RAM). Good agreement with measurements is also seen for this case which approaches the limiting zero-modeling-error situation of $\lambda \to \infty$.

The quadrature and empirical models presented here are easy to understand and use. The weighted average models are much more complicated and generally require a program to compute it, but they are potentially more accurate and could have more general application as a theoretical tool. We have provided online versions of these calculators on the world wide web [35].

Table 6
Summary of radial and time-of-flight (TOF) fractional errors (FE) evaluated for trajectories following deflection through $\omega = 180^\circ$ in the spherical capacitor (SC) described in Table 1

				A (2-D)[a] 1[b]	B (2-D)[a] 10[b]	C (3-D)[a] 1[b]
Trajectories ($\alpha = 0^\circ$)				(-82.205×10^{-4})	(-12.170×10^{-4})	(-159.06×10^{-4})
Radius:	Orbit	r_0(mm)	$r_{\pi\,\mathrm{exact}}$ (mm)	$FE_{r\,\pi} = (r_{\pi\,\mathrm{sim}} - r_{\pi\,\mathrm{exact}})/r_{\pi\,\mathrm{exact}}\,(\times 10^{-4})$		
	I	81.6	81.6	−50.2	−10.2	−36.4
	II	101.6	101.6	-84.3 ± 8	-12.7 ± 0.2	-127.0 ± 2
	III	121.6	121.6	−95.6	−13.7	−134.1
TOF:	Orbit	r_0(mm)	$TOF_{\pi\,\mathrm{exact}}$ (ns)	$FE_{TOF\,\pi} = (TOF_{\pi\,\mathrm{sim}} - TOF_{\pi\,\mathrm{exact}})/TOF_{\pi\,\mathrm{exact}}\,(\times 10^{-4})$		
	I	81.6	12.2493	−49.8	−10.3	−43.1
	II	101.6	17.0183	-83.4 ± 15	-8.5 ± 0.6	-125.5 ± 5
	III	121.6	22.2831	−93.8	−12.9	−122.6
Line shapes ($\lvert\alpha\rvert \le 2^\circ$)						
Peak position:		r_0(mm)	$Peak_{exact}$ (mm)	$FE_{peak} = (peak_{sim} - peak_{exact})/peak_{exact}\,(\times 10^{-4})$		
		81.6	81.6	−50.2	−11.0	−33.1
		101.6	101.6	−85.6	−14.8	−127.0
		121.6	121.6	−96.2	−15.6	−130.8
Base width:		r_0(mm)	bw_{exact} (mm)	$FE_{bw} = (bw_{sim} - bw_{exact})/bw_{exact}\,(\times 10^{-4})$		
		81.6	0.199	126	1	859
		101.6	0.248	202	−20	40
		121.6	0.296	169	−17	567

Details of the circular orbits I, II, III and SIMION SC electrode geometry constructions A, B and C are given in Tables 2 and 3, respectively. The launching radius r_0 and angle α are listed. Typical FE uncertainties ($\pm$) due to trajectory starting point dependence (ω_0—see Fig. 5) are only shown for $FE_{r\,\pi}$ and $FE_{TOF\,\pi}$ of orbit II. The peak positions and base widths of the Monte-Carlo generated line shapes (see Section 5.2.2) are used to determine the corresponding fractional errors. FE_{bw} is indicative of the *relative* FE error. Radial fractional errors determined from either the line shapes or the circular orbits are seen to be practically identical. Model predictions are found to be independent of the launching radius r_0 and give equal FEs for radius and TOF at $\omega = 180^\circ$. Model results are listed in Table 5. The results of our "best" model (the cw-model) are given on the first line of the table in parenthesis for comparison.

[a] Geometry.
[b] λ (gu/mm) .

7. Summary and conclusions

We have investigated the accuracy of the finite difference method (FDM) approach to charged particle optics simulation as exemplified by the popular package SIMION for the case of Kepler orbits in the field of a spherical capacitor. Our primary goal was to characterize, quantify and model inaccuracies in the simulated electron trajectory orbit radius and time-of-flight as a function of orbit radius and angle for different geometrical FDM simulations of the SC electrodes. In particular, we were interested in establishing a quantitative connection between the observed trajectory inaccuracies and the surface coarseness inherent in the modeling of the SC electrodes by the fixed-grid-sized finite difference approach.

We used rather large SCs, having a mean radius $\bar{R} = 101.6$ mm, typical of modern hemispherical deflector analyzers. The SC mean radius was kept fixed throughout the entire investigation so that the central principal ray with pass energy w = 1000 eV always described the same circular trajectory. The interradial SC electrode spacing ρ and SIMION potential array grid unit density λ were also varied under both 2-D and 3-D SIMION representations over a wide range with $\rho = 0.18$–0.97 and λ = 1–10 gu/mm. SIMION results for the potential, electric field, trajectory radius and TOF were evaluated over three specific circular electron radii $r_0 = 81.6, 101.6(= \bar{R}), 121.6$ mm and compared to exact analytic results in the form of fractional errors presented as functions of the orbit angle $\omega = 0$–360°.

Results at $\omega = 180^\circ$ corresponding to the first-order focusing plane of an HDA were examined and summarized in numerical form in Table 6, while Figs. 3–6, and 8 give more detailed information over the entire ω range. FEs are seen to be comparable in value to the ones reported by D. Dahl [3] for a cylindrical mirror analyzer. The Monte-Carlo generation of line shapes at the first-order focus plane ($\omega = 180^\circ$), was found to be a comprehensive way to test both absolute and relative radial accuracy as shown in Fig. 7. Overall, the generated line shapes were also in fair agreement with theory, even though shifted in the absolute radial exit position.

The inaccuracies due to the electric field interpolation and the Runge-Kutta trajectory integration (discussed in Appendix B) were found to be minor compared to the error induced by the finite difference modeling of the curved surfaces by squares or cubes. Comparison of these FEs showed that increasing the grid density λ by a factor of 10 improves the accuracy of the potential, radial electric field, trajectory radius and TOF simulations by roughly the same amount, while the accuracy of kinetic energy error was improved by about three orders of magnitude. 2-D geometries with the highest grid density for trajectories furthest from the electrodes gave the best results. The sensitivity to the launching point starting orbit angle position was also evaluated and found to affect the error by 5–15%.

Finally, these results were generalized using theoretical models that predict the SIMION trajectory FEs in the radius and TOF for any HDA. These models are based on the observations that

the trajectory FEs are mainly due to the small, but significant, electrode surface modeling "errors" ΔR_i with $(i = 1, 2)$. The models explain the electric field perturbation as a small overall constant change Δk (or FE_k) in the ideal $-k/r^2$ electric field constant k. This perturbation in the field then results in the trajectory radius and TOF FEs, which are found to be proportional to FE_k. The models predict trajectory FEs that are approximately independent of the launching radius r_0 and angle ω, in fair overall agreement with the corresponding SIMION FEs for all tested geometries and orbits. Three types of models for predicting FE_k from the individual electrode errors ΔR_i were investigated and found to be successful to various degree of accuracy. All our models correctly predicted the dependence of the radial and TOF FEs on the grid density λ and the interradial electrode spacing ρ for the central ray at $\omega = 180^\circ$ and showed the radius and TOF FEs to be equal at this particular orbit angle in agreement with our simulation results. It was also found that the main source of error can be partly compensated for by removing approximately 0.1–0.2 gu from each spherical surface in the model.

In conclusion, this investigation provides some further insights into the accuracy of field and trajectory calculations and the factors affecting them in the simulation of the spherical electrodes by the finite difference approach and establishes the equations relating the observed fractional errors to the modeling parameters. Our methodology and semi-empirical results should provide useful guidelines for evaluating the accuracy of SIMION in HDA applications and hopefully encourage more such practical benchmark tests, analysis and intercomparisons of existing charged particle optics programs and approaches. The extent to which these results can also be applied to realistic HDA applications with strong fringing fields remains to be seen.

Acknowledgments

We would like to thank David Dahl for very helpful communications regarding the use of SIMION, in particular together with Tony Appelhans, Dezső Varga and Manolis Benis, for their detailed critical comments and suggestions on improving the manuscript. We also thank our colleagues, Xenophon Zotos and John Ekaterinaris, for useful discussions on perturbation and finite-element theory, and Mevlut Doğan for his support and interest in this project. This work was supported by the Greek-Hungarian S&T cooperation GR-11/03 and a travel grant by the University of Crete.

Appendix A. Trajectory equations—connection between SC and HDA

In the main text we presented the trajectory equations in all generality, but limited our SC investigation to the conventional unbiased HDA case where $\tilde{V}_0 \equiv \tilde{V}(R_0) = 0$. Here, we shall obtain the basic trajectory parameters for all HDAs [16].

The voltages $\tilde{V}_1$ and $\tilde{V}_2$ determine the precise trajectory and are set by "tuning" the SC to the *principal* ray. In general, the principal ray for any HDA follows an ellipse entering with $\alpha = 0$ and radius R_0 and exiting after deflection by 180° with radius R_π. Both R_0 and R_π must be externally specified as well as the potential $\tilde{V}_0$. In general, $R_0 \neq R_\pi$ and $\tilde{V}_0 \neq 0$ [16]. For a conventional HDA $R_0 = R_\pi = \bar{R}$ and $\tilde{V}_0 = 0$ and the orbit is a circle. For the general HDA these conditions lead to the following two equations:

$$\frac{R_0}{R_\pi} = \frac{2a_0}{(2a_0 - R_0)} - 1 \tag{A.1}$$

$$\tilde{V}_0 = -\frac{k}{R_0} + c \tag{A.2}$$

with a_0, the semi-major axis of the principal ray. Defining the useful shorthand

$$\xi \equiv \frac{R_\pi}{R_0} \tag{A.3}$$

we then have

$$a_0 = \frac{(R_0 + R_\pi)}{2} = \frac{R_0\,(\xi + 1)}{2} \tag{A.4}$$

Eqs. (A.1) and (A.2) can be solved for k and c utilizing Eqs. (A.4) and (A.3) to obtain:

$$q\,k = K_0\,R_0\,\frac{(\xi + 1)}{\xi} \tag{A.5}$$

$$q\,c = q\,\tilde{V}_0 + K_0\,\frac{(\xi + 1)}{\xi} \tag{A.6}$$

Upon substitution of k and c into Eq. (1) we obtain for $\tilde{V}_i$:

$$q\,\tilde{V}_i = K_0\left[\frac{(\xi + 1)}{\xi}\left(1 - \frac{R_0}{R_i}\right)\right] + q\,\tilde{V}_0 \quad (i = 1, 2) \tag{A.7}$$

From the particle's nominal pass energy t given by [16]:

$$t = E + q\,c = K(r_0) + q\,\tilde{V}(r_0) \tag{A.8}$$

we obtain for $t = \mathrm{w}$ the principal ray tuning energy w:

$$\mathrm{w} = E_0 + q\,c = K_0 + q\,\tilde{V}_0 \tag{A.9}$$

Here we also define γ, the user supplied *biasing* parameter [16], specifying the desired potential at the principal ray starting radius R_0, $\tilde{V}_0 = V(R_0)$:

$$q\,\tilde{V}_0 \equiv (1 - \gamma)\,\mathrm{w} \tag{A.10}$$

For a conventional HDA with $\tilde{V}_0 = 0$, $\gamma = 1$. Defining the reduced HDA pass energy $\tau \equiv t/\mathrm{w}$, we may rewrite all trajectory parameters in terms of γ, ξ, w, τ referenced to the principal ray [16]. Using the shorthand $\kappa \equiv \gamma/\xi$ we have:

$$q\,c = \mathrm{w}\,(1 + \kappa) \tag{A.11}$$

$$q\,k = \mathrm{w}\,R_0\,(1 + \xi)\,\kappa \tag{A.12}$$

$$a = \frac{1}{2}\,R_0\,(\xi + 1)\left[\frac{\kappa}{\kappa + 1 - \tau}\right] \tag{A.13}$$

$$E = -\mathrm{w}\,(1 - \tau + \kappa) \tag{A.14}$$

$$K(r_0) = \mathrm{w}\left\{\tau - 1 + \kappa\left[\frac{R_0}{r_0}\,(1 + \xi) - 1\right]\right\} \tag{A.15}$$

$$q\,\tilde{V}(r_0) = \mathrm{w}\left[\kappa + 1 - \kappa\,(1 + \xi)\,\frac{R_0}{r_0}\right] \tag{A.16}$$

since $E_0 < 0$ for bound motion, we must always have $\gamma > 0$.

The voltages are then given by:

$$q\,\tilde{V}_i = \mathrm{w}\left\{1 - \kappa\left[\frac{R_0\,(1+\xi)}{R_i} - 1\right]\right\} \qquad (i = 1, 2) \qquad \text{(A.17)}$$

If we write the two radii R_1 and R_2 in terms of the mean radius $\bar{R}$ and the interradial electrode spacing $\rho = \Delta R/\bar{R}$, useful in ρ-dependence studies (see Sections 5.4 and 6), we have:

$$R_1 = \bar{R}\,(1 - \rho/2) \qquad \text{(A.18)}$$

$$R_2 = \bar{R}\,(1 + \rho/2) \qquad \text{(A.19)}$$

$$q\,\tilde{V}_1 = \mathrm{w}\left[\kappa + 1 - \frac{2\,\kappa\,(1+\xi)}{(2-\rho)}\left(\frac{R_0}{\bar{R}}\right)\right] \qquad \text{(A.20)}$$

$$q\,\tilde{V}_2 = \mathrm{w}\left[\kappa + 1 - \frac{2\,\kappa\,(1+\xi)}{(2+\rho)}\left(\frac{R_0}{\bar{R}}\right)\right] \qquad \text{(A.21)}$$

$$q\,\Delta\tilde{V} = \frac{4\,\mathrm{w}\,\kappa\,(1+\xi)\,\rho}{(4-\rho^2)}\left(\frac{R_0}{\bar{R}}\right) \qquad \text{(A.22)}$$

We note that the kinetic energy used in SIMION for "flying" a particle with nominal pass energy t is $K(r_0)$ given by Eq. (A.15). When $\tilde{V}(r_0) = 0$, $K(r_0)$ is indeed equal to t (see Eq. (A.8)); however, for $\tilde{V}(r_0) \neq 0$, $K(r_0)$ is in general different from t. This has to do with the convention that kinetic energy is always defined with respect to ground, i.e. zero potential.

In HDAs, there is an extra voltage V_p corresponding to the plate voltage used with pre-retardation. The HDA voltages V_i are then related to the SC voltages $\tilde{V}_i$ by the simple formula:

$$V_i = \tilde{V}_i + V_\mathrm{p} \qquad (i = 1, 2) \qquad \text{(A.23)}$$

The derivation of the HDA trajectories and voltages has been presented in detail in ref. [16]. The above treatment of the SC trajectories and voltages connects the two in a consistent way including the case of the biased paracentric HDA [9,16].

Appendix B. SIMION details

B.1. Geometry (.gem) files

The three geometries A, B and C used to represent the SC electrodes with $R_1 = 72.4$ mm and $R_2 = 130.8$ mm at voltages $V_1 = 806.6298$ V and $V_2 = -446.4832$ V were constructed using the following SIMION geometry files [35]:

Geometry A (2-D, $\lambda = 1$ gu/mm)

```
pa_define(150,150,1,cylindrical,xy)
e(-446.4832){fill{notin{circle(0,0,129.8)}}};OUTER_ELECTRODE_R2=130.8 mm
e(806.6298){fill{within{circle(0,0,72.4)}}};INNER_ELECTRODE_R1=72.4 mm
```

Geometry B (2-D, $\lambda = 10$ gu/mm)

```
pa_define(1500,1500,1,cylindrical,xy)
e(-446.4832){fill{notin{circle(0,0,1307)}}};OUTER_ELECTRODE_R2=130.8 mm
e(806.6298){fill{within{circle(0,0,724)}}};INNER_ELECTRODE_R1=72.4 mm
```

Geometry C (3-D, $\lambda = 1$ gu/mm)

```
pa_define(150,150,150,planar,xyz)
e(-446.4832){fill{notin{sphere(0,0,0,129.8)}}};OUTER_ELECTRODE_R2=130.8 mm
e(806.6298){fill{within{sphere(0,0,0,72.4)}}};INNER_ELECTRODE_R1=72.4 mm
```

Note that we have used radius $R_{2\mathrm{g}} = 129.8$ gu in geometry A and C and $R_{2\mathrm{g}} = 1307$ gu in geometry B. These are 1 gu *smaller* than the theoretical values of R_2, 130.8 and 1308 gu, respectively. This correction is an artifact of the behavior of the *notin* instruction, and the need for it can be seen by measuring the geometry as done in Fig. 2 (bottom). The effect of erroneously including the additional grid unit results in $R_{2\mathrm{g}}$ shifted outward by 1 gu, which does not much affect the magnitude of the FEs but does change their signs, demonstrating the sensitivity to just 1 gu change. In the case of the line shapes, it affects position but imposes negligible differences in the overall shape itself.

B.2. Simulation conditions

All SIMION PAs were refined with a convergence objective of 1×10^{-7} with all other refining parameters left at default. All trajectories were computed with the default value of the trajectory quality control (tqc) parameter (e.g. tqc = +3). Smaller time steps using tqc = 302 had no effect on the trajectories. Particles were flown in the XY-plane launched at $x_0 = r_0$, $y_0 = 0$ and azimuthal angle Azm = 0°, elevation angle El = 0° and velocity elevation angle Elv = −90° with ω increasing from 0 in the clockwise direction. Finally, to avoid relativistic effects not included in our theoretical treatment, a *heavy* electron mass m was used with $m = 10^{12}\,m_\mathrm{e}$. The heavier mass only slows down the particle and thus the appropriate correction factor of 10^{-6} was included in $\mathrm{FE_{TOF}}$ (Eq. (23)).

B.3. FEs in the XY plane with $\mathcal{E}_\mathrm{r}$-field set exactly from theory

Using SIMION programming capabilities (.prg files), the radial electric field could be set to the exact theoretical values, thus bypassing errors introduced by electrode inaccuracies, numerical errors in solving the Laplace equation, and errors produced by interpolating and computing the gradient potential to obtain the electric field. Thus, any non-zero FEs in the trajectory strictly reflect just the Runge-Kutta trajectory integration accuracy. Extremely small FEs were found on the 10^{-7} level or smaller for all variables, clearly demonstrating that trajectory integration errors are indeed negligible. These are not shown due to space limitations.

Table B.1
Comparison of FE values in different planes of motion ($Z = 0$ or $X = 0$) or when using exact theoretical fields in SIMION

Procedure	Geometry	Plane of motion	$r_0 = 81.6$ mm		$r_0 = 101.6$ mm		$r_0 = 121.6$ mm	
			FE_r ($\times 10^{-4}$)	FE_{TOF} ($\times 10^{-4}$)	FE_r ($\times 10^{-4}$)	FE_{TOF} ($\times 10^{-4}$)	FE_r ($\times 10^{-4}$)	FE_{TOF} ($\times 10^{-4}$)
Exact $\vec{\mathcal{E}}$-field (.prg)	ABC	$Z = 0$	0.00123	0.0538	0.000984	0.0536	0.000	0.0536
Exact $\vec{\mathcal{E}}$-field (.prg)	ABC	$X = 0$	0.00123	0.0538	0.000984	0.0536	0.000	0.0536
Exact $\tilde{V}(r)$ (Perl PA)	A	$Z = 0$	−0.6863	−0.794	−0.492	−0.457	−0.329	−0.309
Exact $\tilde{V}(r)$ (Perl PA)	B	$Z = 0$	−0.0123	0.0228	0.000	0.0718	0.000	0.0495
Exact $\tilde{V}(r)$ (Perl PA)	C	$Z = 0$	−0.686	−0.712	−0.492	−0.457	−0.329	−0.309
$\tilde{V}_1$, $\tilde{V}_2$ refine	A	$Z = 0$	−50.25	−49.78	−84.25	−87.13	−95.56	−93.79
$\tilde{V}_1$, $\tilde{V}_2$ refine	B	$Z = 0$	−10.25	−10.26	−12.11	−12.09	−13.65	−12.92
$\tilde{V}_1$, $\tilde{V}_2$ refine	C	$Z = 0$	−36.45	−43.08	−126.97	−125.5	−134.1	−122.6
$\tilde{V}_1$, $\tilde{V}_2$ refine	A	$X = 0$	251.7	277.4	13.58	13.82	198.4	186.0
$\tilde{V}_1$, $\tilde{V}_2$ refine	B	$X = 0$	−4.616	−4.564	−7.330	−7.280	0.1234	0.1765
$\tilde{V}_1$, $\tilde{V}_2$ refine	C	$X = 0$	–	–	−126.8	−125.6	–	–

FEs are measured at $\omega = \pi$ for orbits with $r_0 = 81.6$ mm, $r_0 = 101.6$ mm and $r_0 = 121.6$ mm in geometries A, B and C. The values of $k = -203200$, $c = -2000$, $m = m_e \times 10^{12}$, $R_1 = 72.4$ mm, $R_2 = 130.8$ mm have been used in all calculations.

B.4. FEs in the XY plane with $\tilde{V}(r)$ set exactly from theory

Using external software programming, all cells in SIMION potential arrays can be modified directly. PERL script `sc_make_theoretical_pa.pl` were used to set the PA potentials to the exact theoretical values, thus eliminating electrode modeling errors in the potential except for interpolation errors and errors in computing the electric field from the potential using Eq. (3). In Fig. B.1, we show the resulting FEs to be of the order of 1×10^{-4} (A and C) or 3×10^{-6} (B), which are roughly 100 times smaller than the FEs already shown in Figs. 3 and 4. Some special simulation techniques could take advantage of this fact.

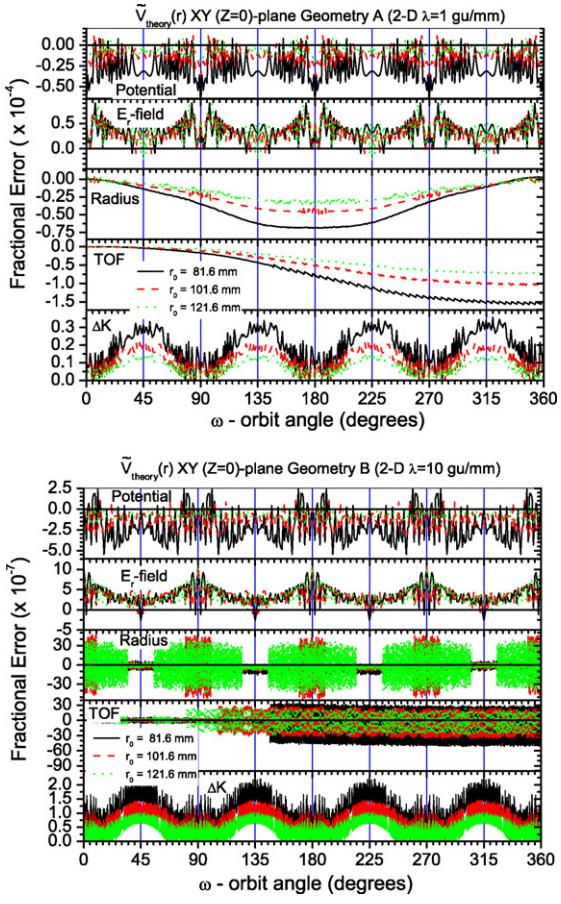

Fig. B.1. (Color on line) Same as Fig. 3 for geometry A (top) and B (bottom), but with the exact theoretical potential inserted into the SIMION potential arrays (via software) rather than setting the voltage on the electrodes and then solving the Laplace equation (SIMION refining). The electrodes in this case have no effect. For geometry C (not shown) FEs are found to be identical to those of A with only the kinetic energy FE being slightly larger.

B.5. FEs for motion in the YZ ($X = 0$) plane

One might argue that the FE results presented in the main text are somewhat contrived and almost worst-case. As already discussed by Dahl [3] by taking advantage of the special symmetries of the problem and using integrally aligned boundaries one can always strive to minimize, or possibly eliminate, the errors in the model. In the case of the 2-D representations of the SC in SIMION, the axis of symmetry is the x-axis, so $R_{i\,\mathrm{sim}}$ values will be constant in the YZ ($X = 0$) plane and no ω dependence will be observed in the fields. Furthermore, those $R_{i\,\mathrm{sim}}$ may be integrally aligned, giving ideally sized electrodes in the $X = 0$ plane. For $\lambda = 1$ (A), we have integer round-off giving $R_{1\,\mathrm{sim}} = 72$ gu and $R_{2\,\mathrm{sim}} = 131$ gu, introducing a constant error in the $X = 0$ plane, but for $\lambda = 10$ (B), we can have $R_{1\,\mathrm{sim}} = 724$ gu and $R_{2\,\mathrm{sim}} = 1308$ gu and integrally aligned boundaries are indeed possible. Motion in the $X = 0$ plane is investigated in Table B.1. In the $X = 0$ plane, FEs are indeed worse in the outer orbits of A and much better in the outer orbits of B (integrally aligned), but B is only marginally better in the central orbit. This limited improvement in the central orbit of B is explainable since even though there are no electrode errors in the $X = 0$ plane, there are unavoidable electrode errors just off the $X = 0$ plane, which do affect the potentials in the $X = 0$ plane. That error was avoided in a cylindrical capacitor used by Dahl. [3].

References

[1] D. Cubric, B. Lencova, F. Read, J. Zlamal, Nucl. Instrum. Methods Phys. Res. A 427 (1999) 357.
[2] F.H. Read, J. Comput. Phys. 133 (1997) 1.

[3] D.A. Dahl, Int. J. Mass Spectrom. 200 (2000) 3.
[4] G. Martinez, R. Becker, Optik 111 (2000) 113.
[5] S.I.S. Inc., SIMION 3D Version 7.0, http://www.simion.com, 2005.
[6] CPO programs, available on the web site http://www.electronoptics.com/.
[7] Available from Vector Fields—software for electromagnetic desing, more information can be found on the web site http://www.vectorfields.com/content/view/26/49/.
[8] O. Sise, M. Ulu, M. Dogan, Nucl. Instrum. Methods Phys. Res. A 554 (2005) 114.
[9] E.P. Benis, T.J.M. Zouros, Nucl. Instrum. Methods Phys. Res. A 440 (2000) 462.
[10] J.H. Vilppola, J.T. Keisala, P.J. Tanskanen, Rev. Sci. Instrum. 64 (1993) 2190.
[11] B. Wannberg, Nucl. Instrum. Methods Phys. Res. A 239 (1985) 269.
[12] A.C. Parr, S.H. Southworth, Nucl. Instrum. Methods Phys. Res. A 222 (1984) 221.
[13] E.P. Benis, et al., Nucl. Instrum. Methods Phys. Res. B 146 (1998) 120.
[14] E.P. Benis, M. Zamkov, P. Richard, T.J.M. Zouros, Phys. Rev. A 65 (2002) 064701.
[15] E.P. Benis, et al., Phys. Rev. A 69 (2004) 052718.
[16] T.J.M. Zouros, E.P. Benis, J. Electron Spectrosc. Relat. Phenom. 125 (2002) 221; ibid. 142 (2005) 175.
[17] V.D. Belov, M.I. Yavor, Nucl. Instrum. Methods Phys. Res. A 470 (2001) 105.
[18] C. Azimonte, et al., Braz. J. Phys. 33 (2003) 788.
[19] M. Cantoni, R. Bertacco, Rev. Sci. Instrum. 75 (2004) 2387.
[20] M. Rachev, R. Srama, A. Srowig, E. Grun, Nucl. Instrum. Methods Phys. Res. A 535 (2004) 162.
[21] D.E. David, D.B. Popović, D. Antic, J. Michl, J. Chem. Phys. 121 (2004) 10542.
[22] D. Desai, et al., J. Res. Natl. Inst. Stand. Technol. 110 (2005) 443.
[23] R. Antoine, et al., Int. J. Mass Spectrom. 239 (2004) 1.
[24] A.D. Appelhans, J.E. Delmore, J.E. Olson, Int. J. Mass Spectrom. 241 (2005) 1.
[25] V. Filip, D. Nicolaescu, M. Tanemura, F. Okuyama, Ultramicroscopy 89 (2001) 39.
[26] W. Knapp, D. Schleubner, Appl. Surf. Sci. 251 (2005) 14.
[27] A.R. Milosavljevic, et al., Meas. Sci. Technol. 16 (2005) 1997.
[28] A.R. Milosavljevic, et al., J. Phys. B 39 (2006) 609.
[29] L. Sarkadi, A. Orban, Meas. Sci. Technol. 17 (2006) 84.
[30] D.A. Dahl, SIMION 3D v6.0, Idaho National Engineering Laboratory, Idaho Falls, 1996.
[31] P.J. Mohr, B.N. Taylor, Rev. Mod. Phys. 77 (2005) 1.
[32] S. Nishigaki, S. Kanai, Rev. Sci. Instrum. 57 (1986) 225.
[33] T. Sagara, L. Boesten, S. Nishida, K. Okada, Rev. Sci. Instrum. 71 (2000) 4201.
[34] David J. Manura, private communications, 2006.
[35] More details can be found at the link http://www.simion.com/tools/sc.